

1 Feb. 28, 2017.

2

3 *Atmos. Chem. Phys.*

4

5 RE: Manuscript Number: acp-2016-732

6

7

8 Dear Editors:

9

10 Thank you very much for your kind decision letter on our paper entitled “**Improving**
11 **PM_{2.5} forecast over China by the joint adjustment of initial conditions and source**
12 **emissions with an ensemble Kalman**” (acp-2016-732). We are grateful for the
13 helpful comments from you and the reviewer. We have changed the manuscript
14 according to his suggestions. We are looking forward to hearing from you soon.

15

16 Sincerely Yours,

17

18 Zhen Peng

19

20 **Response to Reviewer #3's comments:**

21 We thank Reviewer # 3 for his thoughtful comments and suggestions that have helped
22 to improve this manuscript. Our responses to comments (in bold style) and the
23 corresponding changes to the manuscript are detailed below.

24 **I gave went through the manuscript and the authors made a decent effort to try**
25 **to address the issues I raised in my comments. I still have one comment though**
26 **and that is that the authors should be more honest with their results. I'm not**
27 **saying they're hiding information or twisting it around but they should**
28 **acknowledge that for some cases the assimilation just didn't improve things, I'm**
29 **talking about the performance of the assimilation in JJJ. There is some**
30 **improvement in the first 24 hrs but then there is no difference between the**
31 **control run and the forecasts of both experiments. Considering they're focusing**
32 **on the 48hr forecast this is not a minor issue. The authors do mention this in**
33 **section 5.4 but then in the discussions and conclusions they state "Large**
34 **improvements were achieved for almost all the 48-h forecasts, particularly in the**
35 **YRD and PRD. However, relatively smaller improvements were achieved in the**
36 **first 24-h forecast in the JJJ region, which ...". They focus on the 48hrs in the**
37 **analysis of the results and then switch to the 24 hr forecast in the conclusions**
38 **because it did have some improvement. I can understand that the authors want**
39 **to highlight the things that worked in their assimilation, especially after all the**
40 **work they have done, which is really good. All I'm saying is that the authors**
41 **should be honest with the results and if something doesn't work just say so, it**
42 **doesn't make the work less valuable. Based on the results the authors provide,**
43 **the assimilating simply doesn't work for the 48 hr forecast in some regions.**

44 We realized that DA did work for some regions in certain periods although it
45 cannot work perfectly for everywhere at all the time and it shows that there is no
46 difference between the control run and the forecasts of both experiments for the
47 second day forecast in JJJ. So I have replaced "relatively smaller improvements were
48 achieved in the first 24-h forecast in the JJJ region" with "it did show some
49 improvements in the first 24-h but then there is no difference between the control run

50 and the forecasts in the JJJ region afterwards” in Lines 764-766.

51 Also I have added this in the abstract in Line 28 and in section 5.4 in Lines 739.

52

53 **What I also find interesting and the authors didn't address is that based on**
54 **the analysis runs (table 1) there is not much difference in assimilating IC or**
55 **IC+emissions (the authors themselves claim the statistics are the same, I would**
56 **say they are even better for expC in some cases). Anyway, considering that and**
57 **some of the results in figure 10 (in JJJ and YRD during the night), the**
58 **improvement of assimilating emissions in addition to IC seems to be not so big or**
59 **even negligible. I would have expected the authors say something about that as**
60 **well. Is there really a benefit of assimilating both IC and emissions everywhere?**
61 **my answer would be no, but the authors suggest that it is the case, at least imply**
62 **it.**

63 No. Actually the performances of assimilating emission are better in some
64 regions.

65 From Figure 10 we can see that sometimes the performance of expJ was much
66 better than expC in PRD and YRD. We addressed this in Lines 29-32, 722-725,
67 769-771.

68

69 **Last thing, one argument used to explain the performance of the system**
70 **there was the sparsity of the network, but in PRD the network is even sparser**
71 **and the system performs well so I don't see the argument. The authors should**
72 **better explain why in JJJ it is a problem but not in PRD.**

73 In this work, our interested regions were JJJ (36-40 °N, 110-120 °E), YRD (27-35 °
74 N, 116-122 °E) and PRD (22-24 °N, 112-115 °E). There were 12, 24 and 9 stations
75 used for the PM_{2.5} assimilation experiment in JJJ, YRD and PRD respectively. From
76 figure 1 we can see that the measurement coverage in JJJ was much sparser than that
77 in the YRD or PRD. So we think that the sparser coverage of measurements in JJJ
78 may be one of the reasons.

79

80 Some specific comments (based on the version with the modifications highlighted):

81 **Line 705: it says P25, i suppose it should be PM25**

82 In this work, we used P_{25} (the unspiciated aerosol contributions) to calculate
83 $\lambda_{PM_{2.5}}^f$, so it was right in Line 325. We have no special reasons for this. It is also fine
84 to use PM_{25} to calculate $\lambda_{PM_{2.5}}^f$.

85

86 **Line 748-749: What do they mean with “Since we did not know the exact
87 station type,...”, Do they mean urban or rural? please reformulate or clarify. In
88 that same sentence the “We” after the , should be “we”.**

89 We have changed this sentence as “Since we did not know the exact
90 observation environment of the sites,” in Lines 367-368. Also we have replaced
91 “We” with “we”.

92

93 **Lines 1061-1066: As far as I understand the reasons they are providing go in
94 the different direction as what they try to justify. They are addressing the similar
95 performance of the control run and both forecast experiments in YRD during the
96 night. The claim that the prior emissions are larger than the optimized emission
97 during the night and therefore the control run performs worse during night and
98 better during day. What I see in figure 10 is the opposite, the control run
99 performs better during the night than during day. The RMS and bias is smaller
100 during the night than during the day. I would strongly suggest the authors to
101 revise this part.**

102 In this work, the 48-h forecasts were performed at each 0000 UTC from 6 to 16
103 October 2014 with the hourly forecast output for both assimilation experiments. So in
104 Figure 10, daytime starts from 1~11 UTC and 25~35 UTC (corresponding to 9-19
105 Local Time). So it was right in the text and we added the forecasts time in Line 1233.
106 Also we labeled the daytime in Figure 10.

107

108 **Lines 1099-1102: I would ask the authors to reformulate these lines, I’m
109 sure it can be improved.**

110 We have changed these sentences in Lines 727-736.

111

112 **Line 1104: replace “RRD” with "PRD"**

113 We have replaced “RRD” with “PRD” in Lines 738.

114

115

116 **Improving PM_{2.5} forecast over China by the joint adjustment of initial conditions**
117 **and source emissions with an ensemble Kalman filter**

118 Zhen Peng^{1,2}, Zhiquan Liu², Dan Chen², Junmei Ban²

119 1 School of Atmospheric Sciences, Nanjing University, Nanjing, China

120 2 National Center for Atmospheric Research, Boulder, Colorado, USA

121
122 **Abstract.** In an attempt to improve the forecasting of atmospheric aerosols, the
123 ensemble square root filter algorithm was extended to simultaneously optimize the
124 chemical initial conditions and emission input. The forecast model, which was
125 expanded by combining the Weather Research and Forecasting with Chemistry
126 (WRF-Chem) model and a forecast model of emission scaling factors, generated both
127 chemical concentration fields and emission scaling factors. The forecast model of
128 emission scaling factors was developed by using the ensemble concentration ratios of
129 the WRF-Chem forecast chemical concentrations and also the time smoothing
130 operator. Hourly surface fine particulate matter (PM_{2.5}) observations were assimilated
131 in this system over China from 5 to 16 October 2014. A series of 48-h forecasts were
132 then carried out with the optimized initial conditions and emissions on each day at
133 0000 UTC and a control experiment was performed without data assimilation. Besides,
134 we also performed an experiment of pure assimilation chemical ICs and the
135 corresponding 48-h forecasts experiment for comparison. The results showed that the
136 forecasts with the optimized initial conditions and emissions typically outperformed
137 those from the control experiment. In the Yangtze River delta (YRD) and the Pearl
138 River delta (PRD) regions, large reduction of the Root Mean Square Errors (RMSEs)
139 was obtained for almost the entire 48-h forecast range attributed to assimilation.
140 Especially, the relative reduction in RMSE due to assimilation was about 37.5% at
141 nighttime when WRF-Chem performed comparatively worse. In the Beijing–Tianjin–
142 Hebei (JJJ) region, relatively smaller improvements were achieved in the first 24-h
143 forecast **but then no improvements were achieved afterwards**. Comparing to the
144 forecasts with only the optimized ICs, **the forecasts with the joint adjustment were**
145 **always much better during the night in the PRD and YRD regions. However, they**

146 were very similar during daytime in both regions. Also, they performed similarly for
147 almost the entire 48-h forecast range in the JJJ region.

148

149 **1. Introduction**

150 Aerosol prediction by regional air quality model in heavy polluted regions is
151 challenging due to many factors. In addition to the deficiency of chemistries, the
152 uncertainties of primary and precursor emissions and the initial conditions (ICs) also
153 limit the forecast accuracy. Data assimilation (DA), which is used to improve the ICs
154 of aerosols and to optimize data on aerosol emissions, has been shown to be one of
155 the most effective ways to improve the forecasting of aerosol pollution.

156 From the perspective of reducing the uncertainties in the ICs for aerosols, recent
157 efforts have focused on assimilating aerosol observations using optimal interpolation
158 (Collins et al., 2001; Yu et al., 2003; Adhikary et al., 2008; Tombette et al., 2009; Lee
159 et al., 2013) or variational (Kahnert, 2008; Zhang et al., 2008; Benedetti et al., 2009;
160 Pagowski et al., 2010; Liu et al., 2011; Schwartz et al., 2012; Li et al., 2013; Jiang et
161 al., 2013; Saide et al., 2013) DA algorithms. Ensemble-based DA algorithms, such as
162 the ensemble Kalman filter (EnKF) (Sekiyama et al., 2010; Schutgens et al., 2010a,
163 2010b; Pagowski and Grell, 2012; Dai et al., 2014; Rubin et al., 2016; Ying, X.M., et
164 al., 2016; Yumimoto et al., 2016) and the hybrid variational-ensemble DA approach
165 (Schwartz et al., 2014) have also been applied to aerosol predictions. All these studies
166 have shown that DA is one of the most effective ways of improving aerosol
167 forecasting through assimilating aerosol observations from multiple sources (e.g.
168 ground-based observations and satellite measurements) to update the chemical ICs.

169 Numerous studies have used DA approaches to estimate or improve source
170 emissions. The EnKF is one of the most popular DA algorithms used to improve
171 estimates of aerosols and gas-phase emissions, such as NO_x , volatile organic
172 compounds, and SO_2 (van Loon et al., 2000; Heemink and Segers, 2002; Zhang et al.,
173 2005; Barbu et al., 2009; Sekiyama et al., 2010; Huneus et al., 2012; Schutgens et al.,
174 2012; Huneus et al., 2012, 2013; Miyazaki et al., 2014). Variational DA algorithms
175 have also been applied to constrain emissions of air pollution, such as black carbon,

176 organic carbon, dust, NH₃, SO_x and NO_x (Hakami et al., 2005; Elbern et al., 2007;
177 Henze et al., 2007, 2009; Yumimoto et al., 2007, 2008; Dubovik et al., 2008; Wang et
178 al., 2012; Guerrette and Henze, 2015). These studies have indicated that DA can
179 efficiently reduce the uncertainty in the emission inventories and lead to
180 improvements in the forecasting of air quality (Mijling and van der A, 2012).

181 The optimization of chemical ICs and pollution emissions can improve aerosol
182 forecasts and therefore further improvements are likely to be achieved by
183 simultaneously optimizing the chemical ICs and emissions. Tang et al. (2011)
184 reported that the simultaneous adjustment of the ICs of O₃, NO_x and volatile organic
185 compounds and the emissions of NO_x and volatile organic compounds produced
186 overall better performance in both the 1-h and 24-h ozone forecasts than the
187 adjustment of pure ICs or emissions. Miyazaki et al. (2012) reported that the
188 simultaneous adjustment of emissions and concentrations is a powerful approach to
189 correcting the tropospheric ozone budget and profile analyses.

190 We developed a system to adjust the chemical ICs and source emissions jointly
191 within an EnKF system coupled to the Weather Research and Forecasting with
192 Chemistry (WRF-Chem) model (Grell et al., 2005). We then applied this system to
193 assimilate hourly surface PM_{2.5} measurements over China in early October 2014.

194 The remainder of the paper is organized as follows. Section 2 describes this DA
195 system in detail and Section 3 describes the PM_{2.5} observations. Then the
196 experimental designs are introduced in Section 4. Finally, the surface PM_{2.5}
197 observations assimilation results are presented in section 5 before concluding in
198 section 6.

199

200 **2. Methodology**

201 **2.1 Forecast model**

202 For a chemical model like WRF-Chem, the emissions are the model forcing (or
203 boundary condition), rather than model states. Therefore, a forecasting model, **M**,
204 was developed to forecast the emission scaling factors (representing emissions) as
205 well as the aerosol concentrations. This model combines the WRF-Chem model and

206 the forecast model of emission scaling factors.

207

208 2.1.1 WRF-Chem model

209 Version 3.6.1 of the WRF-Chem model (Grell et al., 2005) was used to forecast the
210 aerosol and chemical species. WRF-Chem is an online model with the fully coupled
211 chemical and meteorological components.

212 Most of the WRF-Chem settings were the same as those reported in Liu et al.
213 (2011): the Goddard Chemistry Aerosol Radiation and Transport (GOCART) aerosol
214 scheme coupled with the Regional Atmospheric Chemistry Mechanism for gaseous
215 chemical mechanisms; the WRF single-moment five-class microphysics scheme; the
216 Rapid Radiative Transfer Model longwave and Goddard shortwave radiation schemes;
217 the Yonsei University (YSU) boundary layer scheme; the Noah land surface model;
218 and the Grell-3D cumulus parameterization. For the GOCART aerosol scheme, the
219 aerosol species include 14 defined aerosol species and a 15th variable representing
220 unspatiated aerosol contributions (P_{25}). The 14 defined aerosol species are sulfate,
221 hydrophobic and hydrophilic organic carbon (OC_1 and OC_2 , respectively),
222 hydrophobic and hydrophilic black carbon (BC_1 and BC_2 , respectively), dust in five
223 particle size bins (effective radii of 0.5, 1.4, 2.4, 4.5 and 8.0 μm ; referred to as D_1 ,
224 D_2 , D_3 , D_4 and D_5 , respectively) and sea salt in four particle size bins (effective
225 radii of 0.3, 1.0, 3.25 and 7.5 μm for dry air; referred to as S_1 , S_2 , S_3 and S_4 ,
226 respectively).

227 Figure 1 illustrates the model computational domain. It has 120*120 horizontal
228 grid scales at a 40.5 km spacing by the lambert conform map projection centered at
229 (35°N , 105°E). There are 57 vertical levels with the model top at 10 hPa, about 12
230 layers within the planetary boundary layer (among them the lowest 8 layers were
231 under 500 m), and the first layer centered at ~12 m.

232 With respect to the emissions, the hourly prior anthropogenic emissions were
233 based on the monthly regional emission inventory in Asia (Zhang et al., 2009) for the
234 year 2006 interpolated to the model grid. The power generator emissions were
235 interpolated for the lowest eight vertical levels (Woo et al., 2003; de meij et al., 2006;

236 Wang et al., 2010). Other anthropogenic emissions were assigned totally to the 1st
 237 level. Emissions are very small above 500 m for all pollutants. In order to keep
 238 objective for the prior anthropogenic emissions, no time variation was added. Thus,
 239 the hourly prior anthropogenic emissions were constant. The biogenic (Guenther et al.,
 240 1995), dust (Ginoux et al., 2001), dimethylsulfide and sea salt emissions (Chin et al.,
 241 2000, 2002) were calculated online.

242

243 2.1.2 Forecast model of scaling factors

244 As no suitable dynamic model was available to forecast the emission scaling factors, a
 245 persistence forecasting operator served as the forecast model for the scaling factors,
 246 similar to the method used by Peng et al. (2015) for CO₂ emission inversion. Figure
 247 2a shows the flowchart for the persistence forecasting operator \mathbf{M}_{SF} .

248 If the ensemble members of the updated chemical fields $\mathbf{C}_{i,t-1}^a$ (the subscript i
 249 refers to the i th ensemble member, the superscript a refers to the analysis, and t
 250 refers to the time) and the forecast emissions $\mathbf{E}_{i,t-1}^f$ (the superscript f refers to the
 251 forecast) in the previous assimilation cycle are known, then the chemical fields $\mathbf{C}_{i,t}^f$
 252 at time t can be generated via WRF-Chem (Figure 2b). In the actual process, $\mathbf{C}_{i,t}^f$
 253 were available in the previous assimilation cycle, so we did not need to perform the
 254 ensemble forecasts again. A dotted box was used in Figure 2a to indicate that the
 255 ensemble forecasts were not performed in real process. The ensemble concentration
 256 ratios $\kappa_{i,t}$, ($i = 1, \dots, N$) are then calculated using

$$257 \quad \kappa_{i,t} = \frac{\mathbf{C}_{i,t}^f}{\overline{\mathbf{C}}_t^f}, (i = 1, \dots, N), (1)$$

258 where $\overline{\mathbf{C}}_t^f = \frac{1}{N} \sum_{i=1}^N \mathbf{C}_{i,t}^f$ is the ensemble mean of the forecast. The ensemble mean of
 259 $\kappa_{i,t}$ is,

$$260 \quad \overline{\kappa}_t = \frac{1}{N} \sum_{i=1}^N \kappa_{i,t} = \frac{1}{N} \sum_{i=1}^N \mathbf{C}_{i,t}^f / \overline{\mathbf{C}}_t^f = 1, (2)$$

261 so $\kappa_{i,t}$ are numbers distributed around 1 and with ensemble mean values of 1.

262 The ensemble spreads of $\kappa_{i,t}$, ($i = 1, \dots, N$) may be small and therefore

263 covariance inflation is used to maintain them at a certain level:

$$264 \quad (\boldsymbol{\kappa}_{i,t})_{\text{inf}} = \beta(\boldsymbol{\kappa}_{i,t} - \overline{\boldsymbol{\kappa}_t}) + \overline{\boldsymbol{\kappa}_t}, (i = 1, \dots, N), (3)$$

265 In Peng et al. (2015), the CO₂ DA system worked comparatively well when the
266 ensemble spread of $\lambda_{i,t}^a$ ranged from 0.05 to 1.25 for $\beta = 60, 70, 75, 80$. The
267 assimilated CO₂ fluxes deviated markedly from the “true” CO₂ fluxes when the
268 ensemble spread of $\lambda_{i,t}^a$ were too small for $\beta = 10, 50$ or when the ensemble spread
269 of $\lambda_{i,t}^a$ were too large for $\beta = 100$. Therefore, in this work, $\beta = 1.5$ was chosen to
270 make ensure the ensemble spread of $(\boldsymbol{\kappa}_{i,t})_{\text{inf}}$ ranged from 0.1 to 1.25. Same as $\boldsymbol{\kappa}_{i,t}$,
271 the ensemble mean values of $(\boldsymbol{\kappa}_{i,t})_{\text{inf}}$ are 1. It is noted that perhaps there are very
272 few negative values for $(\boldsymbol{\kappa}_{i,t})_{\text{inf}}$ after inflation. A quality control procedure is
273 performed for $(\boldsymbol{\kappa}_{i,t})_{\text{inf}}$ before further appliance. All these negative data were set as
274 0.001 in this work. There was no special reason to set them as 0.001. It is also fine to
275 set them as 0. Then $(\boldsymbol{\kappa}_{i,t})_{\text{inf}}$ were re-centered to ensure the ensemble mean values of
276 $(\boldsymbol{\kappa}_{i,t})_{\text{inf}}$ were all 1.

277 As the concentrations were closely related to the emissions both locally and in
278 the upwind regions and there is no suitable dynamic model available to forecast the
279 emission scaling factors, the inflated concentration ratios $(\boldsymbol{\kappa}_{i,t})_{\text{inf}}$ serve as the prior
280 emission scaling factors $\boldsymbol{\lambda}_{i,t}^p$:

$$281 \quad \boldsymbol{\lambda}_{i,t}^p = (\boldsymbol{\kappa}_{i,t})_{\text{inf}}, (i = 1, \dots, N), (4)$$

282 The above equation is not supported according to the mass conservation equation
283 but just for the purpose to generate the ensemble emissions. Same as $(\boldsymbol{\kappa}_{i,t})_{\text{inf}}$, $\boldsymbol{\lambda}_{i,t}^p$
284 are numbers distributed around 1. From the perspective of generating the ensemble
285 emissions, they can play the same role as other data, such as the random numbers
286 created by using the standard normal distribution function. However, there are
287 correlations among the grid-points of $(\boldsymbol{\kappa}_{i,t})_{\text{inf}}$ because $(\boldsymbol{\kappa}_{i,t})_{\text{inf}}$ are calculated
288 through a short-term forecast of WRF-Chem. Thus, $\boldsymbol{\lambda}_{i,t}^p$ have the same correlations
289 as $(\boldsymbol{\kappa}_{i,t})_{\text{inf}}$. While, the random numbers are totally different. There are no

290 correlations unless they are generated under certain correlations.

291 To incorporate the useful information from the previous times, the previous DA
292 cycles' analysis scaling factors, $\lambda_{i,t-M+1}^a, \dots, \lambda_{i,t-2}^a, \lambda_{i,t-1}^a$ and the prior scaling
293 factor $\lambda_{i,t}^p$ were used to estimate $\lambda_{i,t}^f$ by the time smooth operator; namely,

$$294 \lambda_{i,t}^f = \frac{1}{M} \left(\sum_{j=t-M+1}^{t-1} \lambda_{i,j}^a + \lambda_{i,t}^p \right), (i = 1, \dots, N, j = t - M + 1, \dots, t - 1), (5)$$

295 Here, M is the time window of the smooth operator. In this study, a value of $M = 4$
296 (hours) was chosen. According to the smooth operator, the ensemble mean values of
297 $\lambda_{i,t}^f$ depend on the ensemble mean of $\lambda_{i,t-M+1}^a, \dots, \lambda_{i,t-2}^a, \lambda_{i,t-1}^a, \lambda_{i,t}^p$, where the
298 ensemble means of $\lambda_{i,t}^p$ are all 1. After multiple iterations, the smooth operator can
299 give comparatively good estimation for $\lambda_{i,t}^f$ since anthropogenic emissions are stable
300 at a certain time scale (Mijling et al., 2012). It is a compromise between prescribed
301 prior emissions and letting the system propagate all observation information from one
302 step to the next without any guidance (Peters et al., 2007), for the case $M = 4$.

303 The ensemble members of the emissions were calculated according to

$$304 \mathbf{E}_{i,t} = \lambda_{i,t} \mathbf{E}_t^p, (i = 1, \dots, N), (6)$$

305 where $\mathbf{E}_{i,t}$ is the i th ensemble member of the emissions for each grid at time t , $\lambda_{i,t}$
306 represents the scaling factors and \mathbf{E}_t^p is the prescribed emission, which can be
307 obtained from the emission inventories. It is noted that the correlations among the
308 grid-points of the prior emissions depend on $\lambda_{i,t}^p$. These correlations may deviate far
309 from the truth but we have no other suitable substitute. However, the correlations
310 among the grid-points of the forecast emissions should be more or less close to the
311 truth due to the appliance of the smooth operator after multiple iterations.

312 It is noted although the method is very similar to that used by Peters et al. (2007)
313 and Peng et al. (2015) for CO₂ emission inversion, it is still of novelty for applications
314 in aerosol anthropogenic emissions. In Peters et al. (2007), $\lambda_{i,t}^p$ were all 1. And only
315 natural CO₂ emissions (i.e., biospheric and oceanic emissions) were assimilated at the
316 ecological scale due to the 'signal-to-noise' problem. Thus, the uncertainty of

317 anthropogenic and other CO₂ emissions were ignored. Besides, the framework is more
318 advanced compared to our previous work. In Peng et al. (2015), in order to generate
319 $\lambda_{i,t}^p$, a set of ensemble forecasts were performed from time t to $t+1$ to produce the CO₂
320 concentration fields, forced by the prescribed net CO₂ surface fluxes with the previous
321 assimilated concentration fields as initial conditions. That means that the ensemble
322 forecast were performed twice in that DA system and it was time consuming.
323 However, in order to save computing time, we used the chemical fields $C_{i,t}^f$ available
324 in the previous assimilation cycle to calculate $\lambda_{i,t}^p$ in this work. Thus, WRF-Chem
325 runs to forecast only once during a DA cycle.

326

327 **2.2 Ensemble square root filter**

328 The ensemble square root filter (EnSRF) algorithm was introduced by Whitaker
329 and Hamill (2002) and its expansion to analyzing aerosol ICs was described by
330 Schwartz et al. (2014). The traditional EnKF with perturbed observations (Evensen
331 1994) introduces sampling errors by perturbing the observations. In contrast to the
332 traditional EnKF, the EnSRF (Whitaker and Hamill, 2002) and the Ensemble
333 Adjustment Kalman Filter (EAKF, developed by Anderson, 2001) obviate the need to
334 perturb the observations. The local ensemble Kalman filtering (LEKF), a kind of
335 EnSRF, was presented by Ott et al. (2002, 2004). It was computationally more
336 efficient compared to the traditional EnKF, since it simultaneously assimilates the
337 observations within a spatially local volume independently. The local Ensemble
338 Transform Kalman Filter (LETKF, Hunt, 2007) integrates the advantages of the
339 Ensemble Transform Kalman Filter (ETKF, developed by Bishop et al., 2001) and the
340 LEKF. The computational cost of LETKF is much lower than that of the original
341 LEKF because the former does not require an orthogonal basis. Though LETKF has
342 more advantages, we still chose the same EnSRF as Schwartz et al. (2014) because we
343 did not need to extend it to analyzing aerosol ICs, very similar to Schwartz et al.
344 (2014).

345 Following the notation of Ide et al. (1997), given an m -dimensional background

346 model forecast vector \mathbf{x}^b , a p -dimensional observation vector \mathbf{y}^o and an operator \mathbf{H}
 347 that converts the model state to the observation states, we expressed the variables as
 348 an ensemble mean (denoted by an over-bar) and a deviation from the mean (denoted
 349 by a prime). Thus, the ensemble mean $\bar{\mathbf{x}}^a$ of the analyzed state \mathbf{x}^a and the
 350 deviations \mathbf{x}'^a from the ensemble mean are updated separately by

$$351 \quad \bar{\mathbf{x}}^a = \bar{\mathbf{x}}^b + \mathbf{K}(\mathbf{y}^o - \mathbf{H}\bar{\mathbf{x}}^b), \quad (7)$$

$$352 \quad \mathbf{x}'^a = \mathbf{x}'^b + \tilde{\mathbf{K}}(\mathbf{y}'^o - \mathbf{H}\mathbf{x}'^b), \quad (8)$$

353 where \mathbf{K} is the traditional Kalman gain matrix and $\tilde{\mathbf{K}}$ is the gain used to update the
 354 deviations from the ensemble mean. These are given by

$$355 \quad \mathbf{K} = \mathbf{P}^b \mathbf{H}^T (\mathbf{H} \mathbf{P}^b \mathbf{H}^T + \mathbf{R})^{-1}, \quad (9)$$

$$356 \quad \begin{aligned} \tilde{\mathbf{K}} &= \mathbf{P}^b \mathbf{H}^T \left[\left(\sqrt{\mathbf{H} \mathbf{P}^b \mathbf{H}^T + \mathbf{R}} \right)^{-1} \right]^T \left(\sqrt{\mathbf{H} \mathbf{P}^b \mathbf{H}^T + \mathbf{R}} + \sqrt{\mathbf{R}} \right)^{-1} \\ &= \left(\mathbf{1} + \sqrt{\mathbf{R} / (\mathbf{H} \mathbf{P}^b \mathbf{H}^T + \mathbf{R})} \right)^{-1} \mathbf{K}, \quad (10) \end{aligned}$$

357 where $\mathbf{P}^b = \frac{1}{N-1} \sum_{i=1}^N \mathbf{x}'^b (\mathbf{x}'^b)^T$ is the $m * m$ -dimensional background error
 358 covariance matrix and \mathbf{R} is the $p * p$ -dimensional diagonal observation error
 359 covariance matrix. In real applications, $\mathbf{P}^b \mathbf{H}^T$ and $\mathbf{H} \mathbf{P}^b \mathbf{H}^T$ will be approximated
 360 using the background ensemble; namely,

$$361 \quad \mathbf{P}^b \mathbf{H}^T = \frac{1}{N-1} \sum_{i=1}^N \mathbf{x}'^b (\mathbf{H} \mathbf{x}'^b)^T \quad (11)$$

$$362 \quad \mathbf{H} \mathbf{P}^b \mathbf{H}^T = \frac{1}{N-1} \sum_{i=1}^N \mathbf{H} \mathbf{x}'^b (\mathbf{H} \mathbf{x}'^b)^T. \quad (12)$$

363 In equations (11) and (12), N is the ensemble size.

364 Note that for the joint analysis of ICs and emissions, the state vector \mathbf{x} is the
 365 joint vector of the mass concentration \mathbf{C} and the emission scaling factor $\boldsymbol{\lambda}$, i.e.
 366 $\mathbf{x} = [\mathbf{C}, \boldsymbol{\lambda}]^T$. In this study, the state variables of the analysis of the ICs were the 15
 367 WRF-Chem/GOCART aerosol variables, same as that reported by Schwartz et al.
 368 (2012). The state variables of the emission scaling factors include $\boldsymbol{\lambda}_{\text{PM}_{2.5}}$, $\boldsymbol{\lambda}_{\text{SO}_2}$, $\boldsymbol{\lambda}_{\text{NO}}$
 369 and $\boldsymbol{\lambda}_{\text{NH}_3}$ and are described in section 2.3.1. After each ensemble analysis, the
 370 ensemble forecasts were performed with the corresponding models to advance \mathbf{C} and
 371 $\boldsymbol{\lambda}$ to the next analysis time.

372 In this work, a 50-member ensemble was chosen, following Schwartz et al.

373 (2012) and Whitaker and Hamill (2002). Covariance localization forced EnSRF
 374 analysis increments to zero 1280 km from an observation in the horizontal and one
 375 scale height to reduce spurious correlations due to sampling error for all control
 376 variables, similar to Pagowski et al., (2012) and Schwartz et al., (2012, 2014). In
 377 addition, posterior (after assimilation) multiplicative inflation following Whitaker and
 378 Hamill (2012) was applied aiming to maintain ensemble spread for only the
 379 concentration analysis. The inflation factor $\alpha = 1.2$ was chosen as Pagowski et al.,
 380 (2012) and Schwartz et al., (2012, 2014). Additive or prior inflation was not employed.
 381 As for the emission scaling factor λ , the inflation was not used at this step.

382

383 **2.3 Data assimilation system**

384 2.3.1 State variables

385 As stated in section. 2.2, the state variables of the analysis of the ICs were the 15
 386 WRF-Chem/GOCART aerosol variables. The $\text{PM}_{2.5}$ observation operator was the
 387 same as that described by Schwartz et al. (2012) and expressed as

$$\mathbf{y}^f = \rho_d[\mathbf{P}_{25} + 1.375\mathbf{S} + 1.8(\mathbf{OC}_1 + \mathbf{OC}_2) + \mathbf{BC}_1 + \mathbf{BC}_2 \\ + \mathbf{D}_1 + 0.286\mathbf{D}_2 + \mathbf{S}_1 + 0.942\mathbf{S}_2], \quad (13)$$

388

389 where ρ_d represents the dry air density, which is multiplied by the mixing ratios of
 390 aerosol species (in $\mu\text{g}\cdot\text{kg}^{-1}$) to convert the units to $\mu\text{g m}^{-3}$ for consistency with the
 391 observations.

392 From the perspective of the optimization of emissions, four species of emission
 393 scaling factors ($\lambda_{\text{PM}_{2.5}}$, λ_{SO_2} , λ_{NO} and λ_{NH_3}) were also considered as the state
 394 variables of the DA system. Atmospheric inorganic aerosols are not only from the
 395 primary emissions, but also from secondary processes- chemical and thermodynamic
 396 transformations from the gas-phase precursors. Therefore, not only the primary
 397 sources of $\text{PM}_{2.5}$, but also the sources of the gas-phase precursors, need to be
 398 optimized. In this study, the sources of SO_2 , NO_x and NH_3 (\mathbf{E}_{SO_2} , \mathbf{E}_{NO} and \mathbf{E}_{NH_3}),
 399 which have a large impact on the distribution of $\text{PM}_{2.5}$, were also optimized in
 400 addition to the primary sources of $\text{PM}_{2.5}$. It is noted that for the optimization of the
 401 emission scaling factors, \mathbf{M}_{SF} serves as the forecast model and the observation

402 operator reflects the combined information of emissions (in the format of λ in
 403 equation (6)), the physics and chemistry processes in WRF-Chem simulations and the
 404 transformation $PM_{2.5}$ from model space to observation space (equation (13)).

405 The direct sources of $PM_{2.5}$ include the unspciated primary sources of $PM_{2.5}$
 406 $E_{PM_{2.5}}$, sulfate E_{SO_4} , nitrate E_{NO_3} , organic compounds E_{org} and elemental
 407 compounds E_{BC} ; all of them are given in two modes (the nuclei and accumulation
 408 modes, represented as i and j in the subscripts respectively). The ratios between the
 409 nuclei and accumulation modes were the same as in the suggested emission process
 410 for National Emission Inventory in WRF-Chem (Freitas et al., 2011). The formula of
 411 sulfate and nitrate emissions in the model are as below:

$$412 \quad E_{PM_{2.5}i} : E_{PM_{2.5}j} = 1 : 4, (14)$$

$$413 \quad E_{SO_4i} : E_{SO_4j} = 1 : 4, (15)$$

$$414 \quad E_{NO_3i} : E_{NO_3j} = 1 : 4, (16)$$

$$415 \quad E_{SO_4i} + E_{SO_4j} = a * (E_{PM_{2.5}i} + E_{PM_{2.5}j} - E_{EC} - E_{ORG}), (17)$$

$$416 \quad E_{NO_3i} + E_{NO_3j} = b * (E_{PM_{2.5}i} + E_{PM_{2.5}j} - E_{EC} - E_{ORG}), (18)$$

417 where E_{EC} represents elemental carbon and E_{ORG} organic compounds, and
 418 $a = 0.074$ and $b = 0.038$ were chosen based on the internal emissions and
 419 observational data. In the DA process, the first 6 species of direct sources of
 420 emissions ($E_{PM_{2.5}i}$, $E_{PM_{2.5}j}$, E_{SO_4i} , E_{SO_4j} , E_{NO_3i} , and E_{NO_3j}), which may have
 421 larger uncertainties in heavy polluted events, were updated according to the variation
 422 of $\lambda_{PM_{2.5}}$. $E_{PM_{2.5}i}$ and $E_{PM_{2.5}j}$ were directly updated according to the variation in
 423 $\lambda_{PM_{2.5}}$. The emissions (E_{SO_4i} , E_{SO_4j} , E_{NO_3i} and E_{NO_3j}) were also updated according
 424 to the variations in $E_{PM_{2.5}i}$ and $E_{PM_{2.5}j}$.

425 E_{EC} and E_{ORG} of the anthropogenic emissions were not assimilated, which is a
 426 limitation in this work. Besides, emissions of dust and sea salt were not assimilated. It
 427 is true that these emissions are also important for the atmosphere aerosol. The reason
 428 we did not assimilate E_{EC} and E_{ORG} is that only the $PM_{2.5}$ measurements are used in
 429 this DA experiment. However, the sources of the aerosols (especially organic aerosols)

430 are so complex that our knowledge of their formation mechanisms is far from clear.
431 Though it is technically possible to have all emissions assimilated, with such limited
432 observations adding more control variables would cause much more uncertainties in
433 the system which might lead to unreasonable analysis.

434

435 2.3.2 Procedure for the DA system

436 Figure 2 (b) shows the workflow of the DA system. The steps in this workflow are as
437 follows.

438 (1) The persistence forecasting operator \mathbf{M}_{SF} is applied to forecast the
439 background fields of the emission scaling factors $\lambda_{PM2.5}^f$, $\lambda_{SO_2}^f$, λ_{NO}^f and $\lambda_{NH_3}^f$. The
440 forecast chemical fields of P_{25} , SO_2 , NO and NH_3 of the previous assimilation cycle
441 are used to create the prior emission scaling factors $\lambda_{PM2.5}^p$, $\lambda_{SO_2}^p$, λ_{NO}^p and $\lambda_{NH_3}^p$.
442 The background scaling factors are then generated using equation (5).

443 (2) The ensemble members of the emissions, $\mathbf{E}_{PM2.5i}^f$, $\mathbf{E}_{PM2.5j}^f$, $\mathbf{E}_{SO_2}^f$, \mathbf{E}_{NO}^f and
444 $\mathbf{E}_{NH_3}^f$, are prepared according to equation (6). The corresponding emissions of $\mathbf{E}_{SO_4i}^f$,
445 $\mathbf{E}_{SO_4j}^f$, $\mathbf{E}_{NO_3i}^f$ and $\mathbf{E}_{NO_3j}^f$ are obtained based on equations (15–18). Other inorganic
446 species of the anthropogenic emission, such as \mathbf{E}_{EC} and \mathbf{E}_{ORG} , are not perturbed for
447 WRF-Chem. However, other anthropogenic emissions, such as $\mathbf{E}_{PM2.5}$, \mathbf{E}_{SO_4} and
448 \mathbf{E}_{NO_3} , are much larger than \mathbf{E}_{EC} and \mathbf{E}_{ORG} in most area of China, and the ensemble
449 spreads of the aerosol concentrate largely dependent on the uncertainties of those
450 anthropogenic emissions. Besides, model errors raised from the meteorology, the
451 emission and the chemical model itself are compensated to some extent through the
452 use of multiplicative inflation. In other words, the ensemble spread of the
453 concentrations can be kept at a certain level though \mathbf{E}_{EC} and \mathbf{E}_{ORG} , are not
454 perturbed.

455 Natural emissions, such as dust and sea salt emissions were not perturbed
456 explicitly when the forecast emissions were generated. However, emissions of dust
457 and sea salt were parameterized within the GOCART model (Chin et al., 2002).
458 Within the DA system, varying meteorology across the members implicitly perturbed

459 dust and sea salt emissions.

460 (3) Forced by the changed emissions ($\mathbf{E}_{\text{PM}_{2.5}i}$, $\mathbf{E}_{\text{PM}_{2.5}j}$, \mathbf{E}_{SO_2} , \mathbf{E}_{NO} , \mathbf{E}_{NH_3} ,
461 $\mathbf{E}_{\text{SO}_4i}$, $\mathbf{E}_{\text{SO}_4j}$, $\mathbf{E}_{\text{NO}_3i}$ and $\mathbf{E}_{\text{NO}_3j}$ were substituted by $\mathbf{E}_{\text{PM}_{2.5}i}^f$, $\mathbf{E}_{\text{PM}_{2.5}j}^f$, $\mathbf{E}_{\text{SO}_2}^f$, \mathbf{E}_{NO}^f ,
462 $\mathbf{E}_{\text{NH}_3}^f$, $\mathbf{E}_{\text{SO}_4i}^f$, $\mathbf{E}_{\text{SO}_4j}^f$, $\mathbf{E}_{\text{NO}_3i}^f$ and $\mathbf{E}_{\text{NO}_3j}^f$; the other emissions such as \mathbf{E}_{EC} and \mathbf{E}_{ORG}
463 remained unchanged), WRF-Chem is run again to forecast the chemical fields ρ^f
464 with the updated chemical fields of the previous assimilation cycle as the ICs. The
465 state variables, i.e., 15 aerosol species and four scaling factors, are then prepared.

466 (4) The model-simulated $\text{PM}_{2.5}$ concentration at the observation space is then
467 calculated via equation (13). At this time, the state vector $\mathbf{x}^f = [\mathbf{C}^f, \boldsymbol{\lambda}^f]^T$ was
468 prepared.

469 (5) In the assimilation step, the state variables, the concentrations of 14 defined
470 aerosol species and a 15th unspciated aerosol, and the four species of emission
471 scaling factors $\boldsymbol{\lambda}_{\text{PM}_{2.5}}^f$, $\boldsymbol{\lambda}_{\text{SO}_2}^f$, $\boldsymbol{\lambda}_{\text{NO}}^f$ and $\boldsymbol{\lambda}_{\text{NH}_3}^f$, were optimized through EnSRF.

472 (6) After the assimilation step, the optimized emissions ($\mathbf{E}_{\text{PM}_{2.5}i}^a$, $\mathbf{E}_{\text{PM}_{2.5}j}^a$, $\mathbf{E}_{\text{SO}_2}^a$,
473 \mathbf{E}_{NO}^a , $\mathbf{E}_{\text{NH}_3}^a$, $\mathbf{E}_{\text{SO}_4i}^a$, $\mathbf{E}_{\text{SO}_4j}^a$, $\mathbf{E}_{\text{NO}_3i}^a$ and $\mathbf{E}_{\text{NO}_3j}^a$) were calculated according to equations
474 (6, 15–18) using the optimized scaling factors ($\boldsymbol{\lambda}_{\text{PM}_{2.5}}^a$, $\boldsymbol{\lambda}_{\text{SO}_2}^a$, $\boldsymbol{\lambda}_{\text{NO}}^a$ and $\boldsymbol{\lambda}_{\text{NH}_3}^a$).

475

476 **3. $\text{PM}_{2.5}$ observation data and errors**

477 Hourly averaged surface $\text{PM}_{2.5}$ observations from the Ministry of Environmental
478 Protection of China were assimilated. There were altogether 876 national control
479 measurement sites over China. The $\text{PM}_{2.5}$ observation sites spanned most of central
480 and eastern China but were primarily located in urban and suburban areas. So it
481 always happened that there were more than one observation sites in certain city,
482 which were fall into the same model grid. **Since we did not know the exact**
483 **observation environment of the sites, we** randomly selected one observation site in a
484 city for assimilation experiment and one for verification purposes to ensure that there
485 was at most one assimilated measurements for one model grid. Altogether 77 stations
486 were selected for the $\text{PM}_{2.5}$ assimilation experiment and another 77 independent

487 stations were selected for verification. Figure 1 shows the locations of 77
488 measurement sites used for the PM_{2.5} assimilation experiment and 77 independent
489 sites used for forecast verification.

490 The observation error covariance matrix \mathbf{R} in equation (9) includes
491 contributions from measurement and representation errors. Similar to the work of
492 Schwartz et al. (2012), the measurement error ε_0 is defined as $\varepsilon_0 = 1.5 + 0.0075 * \Pi_0$,
493 where Π_0 denotes the observational values for PM_{2.5} ($\mu\text{g m}^{-3}$). Thus, higher
494 PM_{2.5} values were associated with larger measurement errors. Following Elbern et al.
495 (2007) and Pagowski et al. (2010), Schwartz et al. (2012), the representativeness error
496 ε_r depends on the resolution of the model and the characteristics of the observation
497 locations and is calculated as $\varepsilon_r = r\varepsilon_0\sqrt{\Delta x/L}$, where r is an adjustable parameter
498 (here, $r = 0.5$), Δx is the grid spacing (here, 40.5 km), and L is the radius of
499 influence of an observation (here, L was set to 3 km following Elbern et al. (2007),
500 since we do not know the station type that used in this work). The total PM_{2.5} error (ε_t)
501 is defined as $\varepsilon_t = \sqrt{\varepsilon_0^2 + \varepsilon_r^2}$. The observation errors are assumed to be uncorrelated
502 so that \mathbf{R} is a diagonal matrix.

503 The PM_{2.5} observations were subject to quality control to ensure data reliability
504 before DA. Considering that China has had intense pollution events, PM_{2.5} values
505 larger than $800 \mu\text{g m}^{-3}$ were classified as unrealistic and were not assimilated;
506 observations with the ensemble mean of the first guess departure exceeding 100
507 $\mu\text{g m}^{-3}$ were also omitted, following Schwartz et al. (2012). The numbers of the
508 observations were about 17700. Among them 8 observations were discarded because
509 they were larger than $800 \mu\text{g m}^{-3}$ and 243 (around 1.5%) were discarded due to the
510 latter reasons.

511

512 **4. Experimental design**

513 Two parallel experiments were performed to evaluate the impact of PM_{2.5} DA on the
514 analyses and forecasts of aerosols over China: an assimilation experiment and a
515 control experiment. Both experiments used identical WRF-Chem settings and

516 physical parameterizations.

517

518 4.1 Spin-up ensemble forecast with perturbed Initial and boundary conditions

519 The initialization and spin-up procedures were identical to those reported by
520 Schwartz et al. (2014). The ICs and lateral boundary conditions (LBCs) for the
521 meteorological fields were provided by the National Centers for Environmental
522 Prediction Global Forecast System (GFS).

523 The initial meteorological fields were created at 0000 UTC 1 October 2014 by
524 interpolating the GFS analyses onto the model domain. The 50 ensemble members
525 were then generated by adding Gaussian random noise with a zero mean and static
526 background error covariances (Torn et al., 2006) to the temperature, water vapor,
527 velocity, geopotential height and dry surface pressure fields. The ICs of each member
528 were zero in the initial aerosol fields, representing clean conditions as described by
529 Liu et al. (2011).

530 The LBCs for the meteorological fields were then interpolated from the GFS
531 analyses from 0000 UTC 1 October 2014 to 0000 UTC 16 October 2014 and
532 perturbed similarly to the initial fields at 0000 UTC 1 October 2014. The aerosol
533 LBCs of each member for all experiments were idealized profiles embedded within
534 the WRF/Chem model.

535 Fifty-member emissions were created by adding random noise to the
536 anthropogenic emissions, same as reported by Schwartz et al. (2014),

$$\mathbf{E}_{ip}^*(\eta, t) = \mathbf{E}_p(\eta, t) + \mathbf{W}_{ip} \boldsymbol{\sigma}_p^E(\eta, t)$$

537 where $\mathbf{E}_{ip}^*(\eta, t)$ is the i th ensemble member for the p th emissions variable at the
538 η th grid point and the t th hour, \mathbf{E}_p is the unperturbed emissions. The term $\boldsymbol{\sigma}_p^E$ is
539 the standard deviation of all \mathbf{E}_p values and in the horizontally adjacent points of grid
540 box η at and within 2 h of t . \mathbf{W} is a weight that was randomly drawn from a
541 standard Gaussian distribution and varied for each ensemble member and variable but
542 was spatially and temporally constant. No correlations between emissions variables
543 were considered, which was a limitation of this approach. For possible negative

544 perturbed emissions, they were set as $\mathbf{E}_{ip}^*(\eta, t) = 0.001 * \mathbf{E}_p(\eta, t)$. This will increase
545 the prescribed emissions more or less. However, only very few data were negative. So,
546 this influence can be negligible.

547 Before the first DA cycle, a 50-member ensemble of four-day WRF-Chem
548 forecasts was performed from 0000 UTC 1 October to 2300 UTC 4 October 2014
549 using the perturbed ICs at 0000 UTC 1 October 2014, the corresponding perturbed
550 LBCs and the emissions. Then a 50-member ensemble aerosol forecasts at 0000 UTC
551 5 October 2014 were produced.

552

553 4.2 Assimilation experiments

554 Two DA experiments were performed. One was the pure assimilation of chemical ICs
555 (hereafter expC), the others was the joint adjustment of chemical ICs and source
556 emissions (hereafter expJ). Both DA experiments had same settings except for the
557 emissions. They were conducted from 0000 UTC 5 October 2014 to 0000 UTC 16
558 October 2014. The assimilation cycle interval was 1 h.

559 In the first DA cycle in expJ, the first 50 ensemble chemical fields were drawn
560 from the WRF-Chem ensemble forecasts valid at 0000 UTC 5 October 2014, as
561 described in section 4.1. Using the ensemble aerosol forecasts, the prior emission
562 scaling factors $\lambda_{i,t}^p$ at 2300 UTC 4 October 2014 were calculated. $\lambda_{i,t}^p$ were used
563 directly as $\lambda_{i,t}^f$ for the first 5 assimilation cycles (after 5 assimilation cycles, the
564 system has been initialized, all future scaling factors could be created using the
565 persistence forecasting operator \mathbf{M}_{SF}). Then, the state vector $\mathbf{x}^f = [\mathbf{C}^f, \lambda^f]^T$ was
566 prepared. And after that, the DA cycle started.

567 In expC, the first chemical fields were also drawn from the WRF-Chem
568 ensemble forecasts valid at 0000 UTC 5 October 2014. Then, the state vector
569 $\mathbf{x}^f = [\mathbf{C}^f]^T$ was prepared and the DA cycle started.

570 At the WRF-Chem forecast step of the subsequent assimilation cycles for both
571 experiments, the ICs for the chemical variables of each member were drawn from the
572 updated chemical fields of the previous cycle. The aerosol LBCs of each member for

573 all experiments were idealized profiles embedded within the WRF/Chem model. As
574 for the meteorological ensemble fields, the LBCs were prepared in advance as
575 depicted in section 4.1; the ICs of each member of the meteorological fields were
576 drawn from the forecast meteorological fields of the previous cycle before
577 re-centering with the GFS analysis because we do not do meteorological analysis:

$$578 \quad \boldsymbol{\pi}_{i_{\text{new}}} = \boldsymbol{\pi}_i + (\boldsymbol{\pi}_{\text{GFS}} - \bar{\boldsymbol{\pi}}), (18)$$

579 where $\boldsymbol{\pi}_i$ is the i th member of the forecast meteorological fields of the previous
580 cycle, $\bar{\boldsymbol{\pi}}$ is the ensemble mean of the forecast meteorological fields of the previous
581 cycle, $\boldsymbol{\pi}_{\text{GFS}}$ is the meteorological field interpolated from the GFS analyses and
582 $\boldsymbol{\pi}_{i_{\text{new}}}$ is the new meteorological field used as the IC in WRF-Chem in the next cycle.

583 As stated in the first paragraph in this section, the settings of expC were the same
584 as those in expJ except for the emissions. In expJ, the ensemble anthropogenic
585 emissions were generated by using emission scaling factors. While in expC, the
586 ensemble anthropogenic emissions were prepared by adding random noise, as stated
587 in 4.1.

588

589 4.3 Control experiment

590 The control experiment was conducted for the same period as the assimilation
591 experiment and the simulation cycle period was 1 h, as in the assimilation experiment.
592 The first initial chemical fields were extracted from the ensemble mean valid at 0000
593 UTC 5 October 2014. In the subsequent simulation process, the ICs for the chemical
594 fields were from the previous cycle's 1-h forecast. The LBCs and ICs for the
595 meteorological fields were updated by interpolating the GFS analyses. The emissions
596 were the prescribed emissions \mathbf{E}_t^{D} without any perturbation.

597

598 5. Results

599 Statistics for both expJ and expC were computed using the ensemble mean prior
600 (background) and posterior (analysis) fields (average of the 50-member ensemble).
601 The ensemble performances were first examined. Output from the first day of the

602 cycling DA configurations was excluded from all verification statistics to allow the
603 ensemble fields to “spin up” from the initial ensemble.

604 As the measurement coverage is an important factor that may determine the
605 performance in DA, we primarily focused our attention on the results from three
606 sub-regions with comparatively dense observational coverage (Figure 1): the Beijing–
607 Tianjin–Hebei region (JJJ, 12 stations for assimilation and 12 stations for verification);
608 the Yangtze River delta (YRD, 24 stations for assimilation and 24 stations for
609 verification); and the Pearl River delta (PRD, 9 stations for assimilation and 9 stations
610 for verification).

611

612 5.1 Ensemble performance

613 It is important to assess the ensemble performance for an ensemble-based DA system.
614 In a well-calibrated system, a comparison of the prior ensemble mean
615 root-mean-square error (RMSE) with respect to the observations should equal the
616 prior “total spread” (square root of the sum of ensemble variance and observation
617 error variance) (Houtekamer et al., 2005). Figure 3 shows the time series for the prior
618 ensemble mean RMSE and the total spread for $PM_{2.5}$ aggregated over all observations
619 in the three sub-regions for expJ. It indicates that the magnitudes of both the total
620 spread and the RMSE were influenced by the diurnal cycle and heavy air pollution.
621 Almost all the total spreads were smaller than the RMSE, showing an insufficient
622 spread of $PM_{2.5}$ ensemble forecasts, which is especially evident for heavy polluted
623 period with much larger RMSEs. For expC, the characteristics of the prior ensemble
624 mean RMSE and the total spread for $PM_{2.5}$ were very similar to that for the joint DA
625 experiment.

626 The magnitudes of the ensemble spread of the emission scaling factors of the
627 joint DA experiment were important for emission inversion. They were very stable
628 throughout the ~10 day experiment period, which indicates that \mathbf{M}_{SF} can generate
629 stable artificial data to generate the ensemble emissions. For $\lambda_{PM_{2.5}}^f$, they ranged
630 from 0.25 to 1 in most model area. Figure 3d shows the area-averaged time series

631 extracted from the ensemble spread of $\lambda_{\text{PM}_{2.5}}^f$. It shows that the ensemble spread was
632 stably distributed around 0.5, which indicates that the uncertainty of the ensemble
633 emissions was about 50%.

634

635 5.2 Impact on aerosol ICs

636 To evaluate quantitatively the impact of the ensemble assimilation system on the ICs,
637 the mean errors (bias), RMSEs and correlation coefficient (CORR) of the assimilation
638 experiment and the control run were first analyzed. These statistics were calculated
639 against independent observations over all the analyses from 6 to 16 October 2014.
640 Table 1 shows that the bias magnitudes of the control run were 15.9 and 20.6 $\mu\text{g m}^{-3}$
641 for the YRD and the PRD, respectively, suggesting a significant overestimation of the
642 WRF-Chem aerosol mass in these two sub-regions. However, a significant
643 underestimation of the aerosol mass occurred in the JJJ region, where the model bias
644 was $-18.0 \mu\text{g m}^{-3}$. The RMSEs of the control run were 81.6, 30.6 and 31.8 $\mu\text{g m}^{-3}$ for
645 the JJJ, YRD and PRD regions, respectively. After assimilation, the statistics showed
646 an apparent improvement and the magnitude of the bias and the RMSE decreased for
647 both DA experiment. For expJ, both the maximum bias and the RMSE were obtained
648 in the JJJ region, and were -10.3 and $66.9 \mu\text{g m}^{-3}$, respectively. The CORR increased
649 from 0.79, 0.60, and 0.62 to 0.83, 0.85, and 0.80 for the JJJ, YRD and PRD,
650 respectively. The statistics of expC were very similar to those of expJ. The bias and
651 the RMSE in the JJJ region were -12.2 and $64.0 \mu\text{g m}^{-3}$, respectively. And the CORR
652 were 0.85, 0.80, and 0.80 for the JJJ, YRD and PRD, respectively. These results
653 indicate that the initial $\text{PM}_{2.5}$ fields can be adjusted efficiently by the EnSRF.

654 It is interesting to note that expC has better RMSE and CORR than expJ but poor
655 bias in JJJ. And expC has better bias and RMSE than expJ but poor CORR in PRD.
656 Maybe small number of samples caused the uncertainties of the statics. However, the
657 differences were very small. The analysis of both experiments were very similar.

658 Then the analysis increments (i.e. $\bar{x}^a - \bar{x}^b$) were investigated to show the direct
659 impact of $\text{PM}_{2.5}$ DA. They are determined by both the observation increments and the
660 relative magnitudes of the forecast error and the observation error, based on Equation

661 (7). From Figure 4(a), (e) and (f), the increments of both assimilation experiments
662 were distributed around the observations as expected. However, the impact of
663 assimilating $\text{PM}_{2.5}$ observations was not limited to the areas where observations were
664 located, observations information was also transported to other areas through the
665 WRF-Chem forecast. Besides, the ensemble forecasts also partly contributed to the
666 spatial distribution of the $\text{PM}_{2.5}$ mass. Therefore, the spatial distributions of the $\text{PM}_{2.5}$
667 mass in both assimilation experiments were significantly different from the control
668 run (see Figure 4(b), (c) and(d)), which suggest that assimilation $\text{PM}_{2.5}$ observations
669 impacts greatly on the aerosol ICs. The $\text{PM}_{2.5}$ mass magnitude of both assimilation
670 experiments were smaller than that of the control run at the lowest model level in the
671 YRD, the PRD and in central China. Conversely, positive differences (analysis minus
672 control) were gained in the JJJ region and in northeast China. These indicated the
673 reduction of the overestimation or underestimation of the WRF-Chem simulation over
674 these regions with data assimilation.

675

676 5.3 Impact on emissions

677 To determine the impact of assimilating $\text{PM}_{2.5}$ observations on the chemical emissions,
678 we analyzed the area-averaged time series extracted from the forecast emission
679 scaling factors, the optimized emission scaling factors, the prior emissions and the
680 optimized emissions. Figure 5 shows that $\lambda_{\text{PM}_{2.5}}^f$ were changed along with $\lambda_{\text{PM}_{2.5}}^a$.
681 This indicates that observation information ingested from the previous observations
682 was incorporated through the usage of the time smooth operator.

683 Figure 5 also shows that although the prior emissions $E_{\text{PM}_{2.5}}^p$ had no diurnal
684 variation when the experiments were designed, the optimized $\text{PM}_{2.5}$ scaling factor,
685 $\lambda_{\text{PM}_{2.5}}^a$, showed an obvious variation with time, as did the optimized unspicated
686 primary sources of $\text{PM}_{2.5}$, $E_{\text{PM}_{2.5}}^a$. Moreover, the values of $\lambda_{\text{PM}_{2.5}}^a$ were <1 at almost
687 all times in the YRD and PRD, which resulted that the analyzed emission $E_{\text{PM}_{2.5}}^a$
688 were lower than the prior $\text{PM}_{2.5}$ emissions $E_{\text{PM}_{2.5}}^p$. In the YRD, the prior $E_{\text{PM}_{2.5}}^p$ was
689 about $0.127 \mu\text{g m}^{-2} \text{s}^{-1}$ over all hours. After assimilation, the time-averaged optimized

690 $E_{PM_{2.5}}^a$ decreased to $0.107 \mu\text{g m}^{-2} \text{s}^{-1}$, about 15.6% lower than the prior value. In the
691 PRD, the prior $E_{PM_{2.5}}^p$ was about $0.10 \mu\text{g m}^{-2} \text{s}^{-1}$. The time-averaged optimized
692 $E_{PM_{2.5}}^a$ decreased to $0.066 \mu\text{g m}^{-2} \text{s}^{-1}$, leading to a decrease of 35.0%. However,
693 larger values for the optimized $E_{PM_{2.5}}^a$ were obtained in the JJJ region in three
694 periods, from 1600 UTC 6 October to 0000 UTC 8 October, from 1600 UTC 9
695 October to 0000 UTC 10 October, and from 1600 UTC 13 October to 0000 UTC 15
696 October as a result of the increased optimized scaling factor $\lambda_{PM_{2.5}}^a$. This may have
697 been caused by the burning of crop residues during harvesting in this region (Li et al.,
698 2016), which was not taken into account in the prior emissions. However, the $PM_{2.5}$
699 measurements network was still spatially sparse and heterogeneous in this work.
700 Almost all measurements were located in the city and no data available in the rural.
701 Meanwhile, the crop residues burning always occur in the rural region. Therefore, the
702 $PM_{2.5}$ measurements network can only capture the burning information a few hours
703 later. Hence, although the system is able to detect the emission changes caused by
704 burning events, the time that the system started to show increased scaling factors
705 might be not accurate enough (may shift a few hours later). Maybe a Kalman
706 smoother would have been a better system to solve this problem.

707 The NO , SO_2 and NH_3 emissions were all adjusted to some extent by our DA
708 approach (see Figure 6). The NO emissions increased by 41.3, 43.7 and 20.3% in the
709 JJJ, YRD and PRD regions, respectively. The SO_2 emissions increased by 16.3, 10.0
710 and 18.3% and the NH_3 emissions increased by 16.7, 7.8 and 7.5% in the JJJ, YRD
711 and PRD regions, respectively.

712 Figure 7 shows the spatial distribution of the time-averaged scaling factors
713 $\lambda_{PM_{2.5}}^a$ at the lowest model level over all hours from 6 to 16 October 2014, since the
714 emissions at higher levels were so small that the impact of assimilating $PM_{2.5}$
715 observations was negligible. Figure 8 shows the distribution of $E_{PM_{2.5}}^p$ and the
716 time-averaged differences between the ensemble mean of the assimilation and the
717 prior values.

718 These patterns are consistent with those in Figure 5. Negative differences were

719 obtained in most areas of the YRD and PRD, indicating that the $PM_{2.5}$ DA primarily
720 decreased the $PM_{2.5}$ emissions. Conversely, positive differences were obtained in
721 South Hebei, North Henan and Southeast Shanxi provinces, indicating that DA
722 increased the $PM_{2.5}$ emissions.

723 As the economy in China has developed, the spatiotemporal distribution of
724 emissions has changed as a result of changes in energy consumption, the structure of
725 the energy market and advances in technology. Therefore although this inventory of
726 emissions may have correctly described anthropogenic emissions in 2006 when it was
727 constructed, it is not representative of the anthropogenic emissions in 2014.
728 Theoretically, the assimilated emissions should reduce the uncertainty in the prior
729 emissions as a result of the application of observations. Different from the situations
730 that standard national emission inventories were reported by government in USA,
731 European or other countries, the rapid economic development and complexity of
732 emission sources in China lead to large uncertainties in the current emission
733 inventories even for the latest version. Thus it's impossible for us to conduct the direct
734 evaluation on emissions.

735 Although we had no direct emission observations to evaluate the analyzing
736 emissions, which was a challenging to many emission inversion research teams (e.g.
737 Tang et al, 2011; Miyazaki et al., 2012; Ding et al., 2015; Mclinden et al., 2016; etc.),
738 the improvement of emissions can be verified in terms of two aspect, the diurnal
739 variation and the location of increased emissions. The diurnal variation in the
740 assimilated emissions verified this statement to some extent. Especially in the PRD
741 and YRD, $E_{PM_{2.5}}^a$ in the daytime were always larger than those in the night, which
742 agreed well with Olivier et al. (2003), the WRAP (2006) and Wang et al. (2010). In
743 addition, the locations of the larger values for the optimized $E_{PM_{2.5}}^a$ in the JJJ region
744 was in good agreement with the place of the crop residues burning *traced by the*
745 *environmental satellite of China*. There were 10, 231, 37 and 3
746 crop residue burning spots in Hebei, Henan, Shandong and Shanxi province
747 respectively from 5 to 11 October 2014 and 7, 20, 5 and 21 respectively from 12 to 18
748 October 2014 (Weekly Crop Residue Burning Monitoring Report traced by

749 Environmental Satellite, 2015a, 2015b).

750 However, the analysis emissions are only a mathematical optimum. They are
751 influenced greatly by the model errors and the observation errors. In addition, only
752 surface PM_{2.5} observations were applied in this work, which may lack abundant
753 constraint on the sources of the secondary aerosol precursors. More observations are
754 needed to obtain reliable emissions for the sources of the gas-phase precursors.

755

756 5.4 Verification of aerosol forecasting

757 For the assimilation experiment, 48-h forecasts were performed at each 0000
758 UTC from 6 to 16 October 2014 with the hourly forecast output for both assimilation
759 experiments. For the verification forecasting experiment for expJ (hereafter fcJ), the
760 ensemble mean of the analyzed ICs and emissions of expJ were used in this
761 longer-range model forecast. For the verification forecasting experiment for expC
762 (hereafter fcC), the ensemble mean of the analyzed ICs of expC and the prescribed
763 anthropogenic emissions were used.

764 In order to get a more visualized picture of the impact of DA for both
765 assimilation experiments, time series of the hourly PM_{2.5} extracted from the analysis
766 (AN), the control run (CT) and the hourly output of 48-h forecast (fc24 for the first
767 day forecast and fc48 for the second day forecast) were compared with the
768 observations (OBS) for three megacities Beijing, Shanghai and Guangzhou,
769 respectively (Figure 9). As expected, the time series of the analysis (also the
770 background) were consistent with the observations. The control run showed large
771 deviations from the observations, especially in Shanghai and Guangzhou. Benefit
772 from DA on both the first day and the second day forecasts can be clearly seen.

773 The bias and the RMSE of the surface PM_{2.5} forecasts as a function of forecast
774 range was then calculated against the independent observations for the three
775 sub-regions (Figure 10). Both the bias and the RMSEs of the control run were
776 characterized by the diurnal cycle in the YRD and PRD. The largest errors were seen
777 at 2100 UTC in the YRD (about 29 $\mu\text{g}\cdot\text{m}^{-3}$ for bias and 37 $\mu\text{g}\cdot\text{m}^{-3}$ for RMSEs) and at
778 2300 UTC in the PRD (about 36 $\mu\text{g}\cdot\text{m}^{-3}$ for bias and 41 $\mu\text{g}\cdot\text{m}^{-3}$ for RMSEs), likely

779 indicating significant systematic forecast errors at these times. From 0300 to 0900
780 UTC, the bias (about $1 \mu\text{g}\cdot\text{m}^{-3}$ in the YRD and $-5 \mu\text{g}\cdot\text{m}^{-3}$ in the PRD) and the RMSE
781 values (about $14 \mu\text{g}\cdot\text{m}^{-3}$ in the YRD and $16 \mu\text{g}\cdot\text{m}^{-3}$ in the PRD) were much smaller
782 than at other times in both the YRD and PRD, showing that WRF-Chem performed
783 well during this period. However, in the JJJ region, the bias (about $-20 \mu\text{g}\cdot\text{m}^{-3}$) and
784 the RMSEs (about $50 \mu\text{g}\cdot\text{m}^{-3}$) were always large as a result of a heavy pollution event.
785 After assimilation, both the magnitude of the bias and the RMSEs decreased sharply.
786 Especially in in YRD and PRD, most bias ranged from -5 to $5 \mu\text{g}\cdot\text{m}^{-3}$ and most
787 RMSEs ranged from 11 to $14 \mu\text{g}\cdot\text{m}^{-3}$, further indicating that DA greatly affected the
788 ICs.

789 The improvements in the surface $\text{PM}_{2.5}$ forecasts by the joint adjustment of the
790 ICs and emissions were very large in the YRD and PRD for expJ. Large reduction of
791 the magnitude of the bias and the RMSEs due to assimilation can be seen for almost
792 the entire 48-h forecast range. From 10- to 23-h and from 34- to 47-h, in particular,
793 the relative reduction in RMSE was about 37.5%. However, the DA impact was much
794 smaller for 3- to 9-h forecast ranges, which are at daytime of the first day forecast. In
795 addition, the improvements were nearly negligible in PRD from 27- to 33-h, the
796 daytime of the second day forecast, suggesting that the benefit gained from adjusting
797 the ICs decreased progressively and eventually disappeared with model integration.
798 And the performance was actually deteriorated in YRD during the same time. One of
799 the possible reasons was that chemical model performed sufficiently well during
800 daytime when the boundary layer was unstable and therefore the further improvement
801 was more difficult. And there were always large errors during the night when the
802 boundary layer was stable, so that large improvements could be obtained. The other
803 possible reason can be attributed to the a priori constant emissions. The differences
804 between the optimized $\text{PM}_{2.5}$ emissions and the prior emissions were comparatively
805 small during the day, but the optimized $\text{PM}_{2.5}$ emissions were much smaller than the a
806 prior emissions during the night. So that the control run could performed worse during
807 the night and it could performed well during the day. Given the a priori variable

808 emissions provided, the control run will perform better during the night. Nevertheless,
809 attributed greatly to the large adjustment of chemical emissions, substantial
810 improvements were still achieved from 34- to 47- h. These results revealed that joint
811 adjustment of the ICs and emissions can improve surface $PM_{2.5}$ forecasts up to 48 h in
812 the YRD and PRD.

813 As for expC, it seemed that large improvements in the surface $PM_{2.5}$ forecasts
814 were gained through the adjustment of the ICs in PRD from 10- to 23-h and from 34-
815 to 47-h. Large reduction of the magnitude of the bias and the RMSEs due to
816 assimilation can be seen during this period. The relative reduction in RMSE ranged
817 from 25% to 37.5%. However, the forecasts deviated much from the observations for
818 3- to 9-h and 27- to 33-h forecast ranges. One of the reason may be that the
819 adjustment of the ICs decreased the analysis field too much on the whole since the
820 WRF-Chem forecast aerosol mass was systematically overestimated in PRD (see
821 Figure 4, Figure 9f and Figure 10e). While this aerosol mass overestimation might be
822 also due to the possibly overestimated emissions in some time periods (not all-day
823 long) which are not corrected in the simulation. So the over-adjusted ICs compensated
824 the unadjusted emissions in some period but also lead to the negative biases for the
825 periods when emission is not overestimated or underestimated. The other factor was
826 the diurnal variation. It is very clear that $PM_{2.5}$ mass gradually decreased with time
827 from 0000 UTC to 0008 UTC and then obtained the smallest value. After that it
828 increased with time from 0009 UTC to 0023 UTC obtained the largest value at about
829 0000 UTC. Both reasons led to the systematically underestimation of $PM_{2.5}$ mass of
830 fcC from 3- to 9-h and from 27- to 33-h, though maybe the aerosol ICs were very
831 close to the observations. Therefore, both the magnitude of the bias and the RMSEs of
832 the fcC were larger than those of the control run. In addition, $PM_{2.5}$ forecasts of the
833 fcC were benefit much from the diurnal variation and the adjustment of the ICs from
834 10- to 23-h and from 34- to 47-h. As a consequence, the magnitude of the
835 corresponding bias and the RMSEs of the fcC were smaller than those of the control
836 run. Similar statics characteristics were also gained in YRD. But the improvements
837 were comparatively small from 10- to 23-h and from 34- to 47-h. However, the

838 performance of fcJ was much better than that of fcC during the night in PRD and
839 YRD. While in the daytime, the improvement of expJ seems to be not so big or even
840 negligible. This could be attributed much to the emissions since the ICs of both
841 forecasts were very similar. In the forecast experiment of expC, the emissions were
842 the default monthly anthropogenic emissions. While in the forecast experiment of
843 expJ, the assimilated emissions were much smaller than the default anthropogenic
844 emissions in almost all the night in both regions indicating that the prior emission
845 uncertainties might be the dominating reasons that cause biases between observed and
846 model simulated concentrations in these cases. In the daytime in PRD, the assimilated
847 emissions were a little smaller than the default anthropogenic emissions. But in the
848 daytime in YRD, the assimilated emissions were a little larger than the default
849 anthropogenic emissions for most time (see Figure 5). While those changes between
850 assimilated emissions and prior emissions in the daytime are not as significant as that
851 in the nighttime.

852 Both DA systems did not perform as well in the JJJ region as in the YRD and
853 PRD. Relatively smaller improvements were achieved in the first 24-h forecast but
854 then no improvements were achieved afterwards in JJJ. One possible reason for this
855 result may be systematic errors due to chemistry mechanism in WRF-Chem. The
856 sources of the aerosols are so complex that our knowledge of their formation
857 mechanisms is far from clear and large uncertainties still exist in the model
858 simulations. Chemical transport models have a tendency to underestimate PM
859 concentrations, especially during episodes of heavy pollution (Denby et al., 2007) due
860 to some missing reactions (Wang et al., 2014; Zhang et al., 2015, Zheng et al., 2015;
861 Chen et al., 2016). Another reason can be attributed to the forecast meteorological
862 fields. There were still large uncertainties, especially when boundary layer was stable
863 and the wind speed was very small during episodes of heavy pollution. As a result, a
864 large bias may be obtained in forecasts of heavy pollution given the ICs and emission
865 inventories achieved from the joint assimilation. Another reason may be the sparse
866 coverage of measurements. There were only 12 sites in the JJJ region (Figure 1) and
867 the measurement coverage was much sparser than in the YRD or PRD.

868

869 **6. Summary and Discussion**

870 The EnSRF algorithm was extended to adjust the chemical ICs and the primary
871 and precursor emissions to improve forecasts for surface PM_{2.5}. This system was
872 applied to assimilate hourly surface PM_{2.5} measurements from 5 to 16 October 2014
873 over China. To evaluate the effectiveness of DA, 48-h forecasts were performed using
874 the optimized ICs and emissions, together with a control experiment without DA.
875 Besides, the experiment of pure assimilation chemical ICs and the corresponding 48-h
876 forecasts experiment were also performed for comparison. The results indicated that
877 the forecasts with the optimized ICs and emissions performed much better than the
878 control simulations. Large improvements were achieved for almost all the 48-h
879 forecasts, particularly in the YRD and PRD. However, **it did show some**
880 **improvements in the first 24-h but then there is no difference between the control run**
881 **and the forecasts in the JJJ region afterwards**, which may be attributed to the sparse
882 measurement coverage and the deficiencies in the model system for forecasting heavy
883 pollution. Comparing to the forecasts with only the optimized ICs, the forecasts with
884 the joint adjustment were always much better **during the night in the PRD and YRD**
885 **regions. However, they were very similar during daytime in both regions. And in the**
886 **JJJ region, they performed similarly for almost the entire 48-h forecast range.**

887 There are still some limitations in this study. Firstly, we use the default monthly
888 anthropogenic emissions as the prior emissions and no time variation was added to
889 keep objective, since no resolution of temporal allocations at shorter but critical
890 (e.g., day-of-week, diurnal) scales is available. As shown in earlier work, the constant
891 emissions will worsen the chemical forecasts (de Meij et al., 2006; Wang et al, 2009).
892 For the joint DA system itself, it cannot benefit from the constant prior anthropogenic
893 emissions. But the normalized RMSE in Figure 10g decreased due to the poor
894 forecasts of control run. The control run will perform better when variable emissions
895 within the day are allowed, especially during the night. As a result, the relative
896 reduction in RMSE could not be so large during the night. Secondly, no correlations
897 between emissions variables were considered when perturbing the emissions, which

898 will lead to the reduction of the correlations between the variables. Thus, the chemical
899 forecast will deviate from the truth to some degree. Fortunately, the perturbed
900 emissions were only used in the initialization and spin-up experiment and expC.
901 Therefore, there were no impacts on expJ and the control run except for expC. Thirdly,
902 \mathbf{E}_{EC} and \mathbf{E}_{ORG} are not perturbed in expJ. However, as stated in Sect. 2.3.2, the
903 ensemble spread of \mathbf{OC}_1 and \mathbf{OC}_2 can be kept at a certain level. As a result, \mathbf{OC}_1
904 and \mathbf{OC}_2 changed much contributed to the $\text{PM}_{2.5}$ assimilation in expJ, which
905 suggests that the influence of not perturbing \mathbf{E}_{EC} and \mathbf{E}_{ORG} could be negligible. But,
906 because of the too small magnitudes of \mathbf{BC}_1 and \mathbf{BC}_2 , the differences (assimilation
907 minus control) of \mathbf{BC}_1 and \mathbf{BC}_2 were nearly close to zero. Fourthly, the experiment
908 (expE) where only emissions were assimilated was not included here. But it was still
909 worth to simultaneously assimilate the chemical ICs and emission. For one thing, in
910 expE, the chemical concentrations can be updated by the WRF-Chem model
911 simulations with the assimilated emissions as the initial field in each DA cycle. That
912 means that the 50-member ensemble forecasts were performed twice and it was time
913 consuming. For another, better concentration analysis could be obtained in expJ due
914 to the simultaneous assimilation of ICs and emissions. While in expE, there may be
915 larger uncertainties for the updated chemical concentrations through WRF-Chem due
916 to the deficiency of chemistries and the uncertainties of the ICs. This will lead to
917 larger uncertainties for the emission inversion. Also the improvement of $\text{PM}_{2.5}$
918 forecasts will be limited due to the comparatively poor chemical ICs.

919 This study represents the first step in the simultaneous optimization of chemical
920 ICs and emissions and only surface $\text{PM}_{2.5}$ measurements were assimilated. In future
921 work, gas-phase observations of SO_2 , NO_2 and CO will be used to further improve the
922 performance of this DA system.

923

924 References

- 925 Anderson, J.L.: An Ensemble Adjustment Kalman Filter for Data Assimilation,
926 Mon.Weather Rev., 129, 2884–2903, 2001.
- 927 Adhikary, B., Kulkarni, S., Dallura, A., Tang, Y., Chai, T., Leung, L. R., Qian, Y.,
928 Chung, C. E., Ramanathan, V., and Carmichael, G. R.: A regional scale chemical
929 transport modeling of Asian aerosols with data assimilation of AOD observations
930 using optimal interpolation technique, Atmos. Environ., 42, 8600–8615,
931 doi:10.1016/j.atmosenv.2008.08.031, 2008.
- 932 Barbu, A. L., Segers, A. J., Schaap, M., Heemink, A.W., and Builtjes, P. J. H.: A
933 multi-component data assimilation experiment directed to sulphur dioxide and
934 sulphate over Europe, Atmos. Environ., 43, 1622–1631, 2009.
- 935 Benedetti, A., Morcrette, J., Boucher, O., Dethof, A., Engelen, R., Fisher, M., Flentje,
936 H., Huneeus, N., Jones, L., and Kaiser, J.: Aerosol analysis and forecast in the
937 European Centre for Medium-Range Weather Forecasts Integrated Forecast
938 System: 2. Data assimilation, J. Geophys. Res., 114, D13205,
939 doi:10.1029/2008JD011115, 2009.
- 940 Bishop, C. H., Etherton, B. J., and Majumdar, S. J.: Adaptive sampling with the
941 ensemble transform Kalman filter. Part I: Theoretical aspects, Mon. Weather
942 Rev., 129, 420–436, 2001.
- 943 Chen, D., Liu, Z., Fast, J., and Ban, J.: Simulations of Sulfate-Nitrate-Ammonium
944 (SNA) aerosols during the extreme haze events over Northern China in October
945 2014, Atmos. Chem. Phys. Discuss., doi:10.5194/acp-2016-222, in review, 2016.
- 946 Chin, M., Rood, R. B., Lin, S. J., Muller, J. F., and Thompson, A. M.: Atmospheric
947 sulfur cycle simulated in the global model GOCART: Model description and
948 global properties, J. Geophys. Res.-Atmos., 105, 24671–24687, 2000.
- 949 Chin, M., Ginoux, P., Kinne, S., Torres, O., Holben, B.N., Duncan, B. N., Martin,
950 R.V., Logan, J.A., Higurashi, A., and Nakajima, J.: Tropospheric aerosol optical
951 thickness from the GOCART model and comparisons with satellite and Sun
952 photometer measurements, J. Atmos. Sci., 59(3), 461–483, 2002.
- 953 Collins, W. D., Rasch, P. J., Eaton, B. E., Khattatov, B. V., and J.-F. Lamarque, J.-F.:

954 Simulating aerosols using a chemical transport model with assimilation of
955 satellite aerosol retrievals: Methodology for INDOEX, *J. Geophys. Res.*, 106,
956 7313–7336, 2001.

957 de Meij, A., Krol, M., Dentener, F., Vignati, E., Cuvelier, C., and Thunis, P.: The
958 sensitivity of aerosol in Europe to two different emission inventories and
959 temporal distribution of emissions, *Atmos. Chem. Phys.*, 6, 4287-4309,
960 doi:10.5194/acp-6-4287-2006, 2006.

961 Dai, T., Schutgens, N.A.J., Goto, D. Shi, G.Y., Nakajima, T.: Improvement of aerosol
962 optical properties modeling over Eastern Asia with MODIS AOD assimilation
963 in a global non-hydrostatic icosahedral aerosol transport model, *Environ. Pollut.*,
964 195, 319–329, 2014.

965 Denby, B., Schaap, M., Segers, A.J., Builtjes, P.J.H., Horalek, J.: Comparison of two
966 data assimilation methods for assessing PM10 exceedances on the European
967 scale, *Atmos. Environ.*, 42 (30), 7122–7134, 2007.

968 Ding, J., van der A, R. J., Mijling, B., Levelt, P. F., and Hao, N.: NO_x emission
969 estimates during the 2014 Youth Olympic Games in Nanjing, *Atmos. Chem.*
970 *Phys.*, 15, 9399-9412, doi:10.5194/acp-15-9399-2015, 2015.

971 Dubovik, O., Lapyonok, T., Kaufman, Y. J., Chin, M., Ginoux, P., Kahn, R. A., and
972 Sinyuk, A.: Retrieving global aerosol sources from satellites using inverse
973 modeling, *Atmos. Chem. Phys.*, 8, 209–250, doi:10.5194/acp-8-209-2008, 2008

974 Elbern, H., Strunk, A., Schmidt, H., and Talagrand, O.: Emission rate and chemical
975 state estimation by 4-dimensional variational inversion, *Atmos. Chem. Phys.*, 7,
976 3749–3769, doi:10.5194/acp-7-3749-2007, 2007.

977 Evensen, G.: Sequential data assimilation with a nonlinear quasi-geostrophic model
978 using Monte Carlo methods to forecast error statistics, *J. Geophys. Res.*, 99(C5),
979 10143–10162, 1994.

980 Freitas, S. R.; Longo, K. M.; Alonso, M. F.; Pirre, M.; Marecal, V.; Grell, G.;
981 Stockler, R.; Mello, R. F.; Sánchez Gárcía, M.. PREP-CHEM-SRC 1.0: a
982 preprocessor of trace gas and aerosol emission fields for regional and global
983 atmospheric chemistry models. *Geoscientific Model Development*, v. 4, p.

984 419-433, 2011.

985 Ginoux, P., Chin, M. Tegen, I., Prospero, J. M., Holben, B., Dubovik, O., and Lin,
986 S.-J.: Sources and distributions of dust aerosols simulated with the GOCART
987 model, *J. Geophys. Res.*, 106, 20,255–20,273, doi:10.1029/2000JD000053,
988 2001.

989 Grell, G., Peckham, S. E., Schmitz, R., McKeen, S. A., Frost, G., Skamarock, W. C.,
990 and Eder, B.: Fully coupled “online” chemistry within the WRF model, *Atmos.*
991 *Environ.*, 39, 6957–6975, doi:10.1016/j.atmosenv.2005.04.027, 2005.

992 Guenther, A., Hewitt, C. N., Erickson, D., Fall, R., Geron, C., Graedel, T., Harley, P.,
993 Klinger, L., Lerdau, M., McKay, W., Pierce, T., Scholes, B., Steinbrecher, R.,
994 Tallamraju, R., Taylor, J., and Zimmerman, P.: A global model of natural
995 volatile organic compound emissions, *J. Geophys. Res.*, 100, 8873–8892,
996 doi:10.1029/94JD02950, 1995.

997 Guerrette, J. J. and Henze, D. K.: Development and application of the
998 WRFPLUS-Chem online chemistry adjoint and WRFDA-Chem assimilation
999 system, *Geosci. Model Dev.*, 8, 1857-1876, doi:10.5194/gmd-8-1857-2015,
1000 2015.

1001 Hakami, A., Henze, D. K., Seinfeld, J. H., Chai, T., Tang, Y., Carmichael, G. R., and
1002 Sandu, A.: Adjoint inverse modeling of black carbon during the Asian Pacific
1003 Regional Aerosol Characterization Experiment, *J. Geophys. Res.-Atmos.*, 110,
1004 D14301, doi:10.1029/2004JD005671, 2005.

1005 Heemink, A.W., and Segers, A.J.: Modeling and prediction of environmental data in
1006 space and time using Kalman filtering, *Stoch. Environ. Res. Risk Assess.* 16 (3),
1007 225–240, 2002.

1008 Henze, D. K., Hakami, A., and Seinfeld, J. H.: Development of the adjoint of
1009 GEOS-Chem, *Atmos. Chem. Phys.*, 7, 2413–2433, doi:10.5194/acp-7-2413-2007,
1010 2007.

1011 Henze, D. K., Seinfeld, J. H., and Shindell, D. T.: Inverse modeling and mapping US
1012 air quality influences of inorganic PM_{2.5} precursor emissions using the adjoint
1013 of GEOS-Chem, *Atmos. Chem. Phys.*, 9, 5877–5903,

1014 doi:10.5194/acp-9-5877-2009, 2009.

1015 Houtekamer, P. L., Mitchell, H. L., Pellerin, G., Buehner, M., Charron, M., Spacek, L.,
1016 and Hansen, B.: Atmospheric data assimilation with an ensemble Kalman filter:
1017 Results with real observations, *Mon. Weather Rev.*, 133, 604–620, 2005.

1018 Ide, K., Courtier, P., Ghil, M., and Lorenc, A. C.: Unified notation for data
1019 assimilation: operational, sequential and variational, *J. Meteorol. Soc. Japan*, 75,
1020 181–189, 1997.

1021 Jiang, Z., Liu, Z., Wang, T., Schwartz, C. S., Lin, H.-C., and Jiang, F.: Probing into
1022 the impact of 3DVAR assimilation of surface PM10 observations over China
1023 using process analysis, *J. Geophys. Res. Atmos.*, 118, 6738–6749,
1024 doi:10.1002/jgrd.50495, 2013.

1025 Peters, W., Jacobson, A. R., Sweeney, C., Andrews, A. E., Conway, T. J., Masarie, K.,
1026 Miller, J. B., Bruhwiler, L. M. P., Petron, G., Hirsch, A. I., Worthy, D. E. J., van
1027 der Werf, G. R., Randerson, J. T., Wennberg, P. O., Krol, M. C., Tans, P. P.: An
1028 atmospheric perspective on North American carbon dioxide exchange:
1029 CarbonTracker, *P. Natl. Acad. Sci. USA*, 104, 18925–18930, 2007.

1030 Kahnert, M.: Variational data analysis of aerosol species in a regional CTM:
1031 Background error covariance constraint and aerosol optical observation operators,
1032 *Tellus, Ser. B*, 60, 753–770, doi:10.1111/j.1600-0889.2008.00377, 2008.

1033 Kleist, D. T., Parrish, D. F., Derber, J. C., Treadon, R., Wu, W.-S., and Lord, S.:
1034 Introduction of the GSI into the NCEP global data assimilation system, *Weather
1035 Forecast.*, 24, 1691–1705, 2009.

1036 Huneus, N., Chevallier, F., and Boucher, O.: Estimating aerosol emissions by
1037 assimilating observed aerosol optical depth in a global aerosol model, *Atmos.
1038 Chem. Phys.*, 12, 4585–4606, doi:10.5194/acp-12-4585-2012, 2012.

1039 Huneus, N., Boucher, O., and Chevallier, F.: Atmospheric inversion of SO₂ and
1040 primary aerosol emissions for the year 2010, *Atmos. Chem. Phys.*, 13,
1041 6555–6573, doi:10.5194/acp-13-6555-2013, 2013.

1042 Hunt, B., Kostelich, E., and Szunyogh, I.: Efficient data assimilation for
1043 spatiotemporal chaos: a Local Ensemble Transform Kalman Filter, *Physica D*,

1044 230, 112–126, 2007.

1045 Lee, E.-H., Ha, J.-C., Lee, S.-S., and Chun, Y.: PM10 data assimilation over South
1046 Korea to Asian dust forecasting model with the optimal interpolation method,
1047 Asia-Pacific J. Atmos. Sci., 49(1), 73–85, doi:10.1007/s13143-013-0009-y,
1048 2013.

1049 Li, Z., Zang, Z., Li, Q. B., Chao, Y., Chen, D., Ye, Z., Liu, Y., and Liou, K. N.: A
1050 three-dimensional variational data assimilation system for multiple aerosol
1051 species with WRF/Chem and an application to PM_{2.5} prediction, Atmos. Chem.
1052 Phys., 13, 4265-4278, doi:10.5194/acp-13-4265-2013, 2013.

1053 Li, J., Li, Y., Bo, Y., and Xie, S.: High-resolution historical emission inventories of
1054 crop residue burning in fields in China for the period 1990–2013, Atmos.
1055 Environ., 138, 152–161, 2016.

1056 Liu, Z., Liu, Q., Lin, H. C., Schwartz, C. S., Lee, Y. H., and Wang, T.:
1057 Three-dimensional variational assimilation of MODIS aerosol optical depth:
1058 implementation and application to a dust storm over East Asia, J. Geophys. Res.,
1059 116, D23206, doi:10.1029/2011JD016159, 2011.

1060 Liu, F., Zhang, Q., Tong, D., Zheng, B., Li, M., Huo, H., and He, K. B.:
1061 High-resolution inventory of technologies, activities, and emissions of coal-fired
1062 power plants in China from 1990 to 2010, Atmos. Chem. Phys., 15,
1063 13299-13317, doi:10.5194/acp-15-13299-2015, 2015.

1064 McLinden, C.A., Fioletov, V., Shephard, M.W., Krotkov, N., Li, C., Martin, R.V.,
1065 Moran, M.D., and J. Joiner,: Space-based detection of missing sulfur dioxide
1066 sources of global air pollution, Nat. Geosci., 9, 496–500, doi:10.1038/ngeo2724,
1067 2016.

1068 Mijling, B. and van der A, R. J.: Using daily satellite observations to estimate
1069 emissions of short-lived air pollutants on a mesoscopic scale, J. Geophys. Res.,
1070 117, D17302, doi:10.1029/2012JD017817, 2012.

1071 Miyazaki, K., Eskes, H. J., Sudo, K., Takigawa, M., van Weele, M., and Boersma, K.
1072 F.: Simultaneous assimilation of satellite NO₂, O₃, CO, and HNO₃ data for the
1073 analysis of tropospheric chemical composition and emissions, Atmos. Chem.

1074 Phys., 12, 9545– 9579, doi:10.5194/acp-12-9545-2012, 2012.

1075 Miyazaki, K., Eskes, H. J., Sudo, K., and Zhang, C.: Global lightning NO_x production
1076 estimated by an assimilation of multiple satellite data sets, *Atmos. Chem. Phys.*,
1077 14, 3277–3305, doi:10.5194/acp-14-3277-2014, 2014.

1078 Ott, E., Hunt, B. R., Szunyogh, I., Zimin, A. V., Kostelich, E. J., et al.: Exploiting
1079 local low dimensionality of the atmospheric dynamics for efficient Kalman
1080 filtering, arXiv:physics/0203058, 24 pp., available at:
1081 <http://arxiv.org/abs/physics/0203058v3/>, 2002.

1082 Ott, E., Hunt, B. R., Szunyogh, I., Zimin, A. V., Kostelich, E. J., et al.: A local
1083 ensemble Kalman filter for atmospheric data assimilation, *Tellus A*, 56, 415–428,
1084 2004.

1085 Pagowski, M., Grell, G. A., McKeen, S. A., Peckham, S. E., and Devenyi, D.:
1086 Three-dimensional variational data assimilation of ozone and fine particulate
1087 matter observations: some results using the Weather Research and Forecasting –
1088 Chemistry model and Grid-point Statistical Interpolation, *Q. J. Roy. Meteor. Soc.*,
1089 136, 2013–2024, doi:10.1002/qj.700, 2010.

1090 Pagowski, M., and Grell, G. A.: Experiments with the assimilation of fine aerosols
1091 using an ensemble Kalman filter, *J. Geophys. Res.-Atmos.*, 117, D21302,
1092 doi:10.1029/2012jd018333, 2012.

1093 Peng, Z., Zhang, M., Kou, X., Tian, X., and Ma, X.: A regional carbon data
1094 assimilation system and its preliminary evaluation in East Asia, *Atmos. Chem.*
1095 *Phys.*, 15, 1087–1104, doi:10.5194/acp-15-1087-2015, 2015.

1096 Pope, C. A.: Review: Epidemiological basis for particulate air pollution health
1097 standards, *Aerosol Sci. Tech.*, 32, 4–14, 2000.

1098 Pope, C. A., Burnett, R. T., Thun, M. J., Calle, E. E., Krewski, D., Ito, K., and
1099 Thurston, G. D.: Lung cancer, cardiopulmonary mortality, and long-term
1100 exposure to fine particulate air pollution, *J. Am. Med. Assoc.*, 287, 1132–1141,
1101 2002.

1102 Rubin, J. I., Reid, J. S., Hansen, J. A., Anderson, J. L., Collins, N., Hoar, T. J., Hogan,
1103 T., Lynch, P., McLay, J., Reynolds, C. A., Sessions, W. R., Westphal, D. L., and

1104 Zhang, J.: Development of the Ensemble Navy Aerosol Analysis Prediction
1105 System (ENAAAPS) and its application of the Data Assimilation Research
1106 Testbed (DART) in support of aerosol forecasting, *Atmos. Chem. Phys.*, 16,
1107 3927-3951, doi:10.5194/acp-16-3927-2016, 2016.

1108 Saide, P. E., Carmichael, G. R., Liu, Z., Schwartz, C. S., Lin, H. C., da Silva, A. M.,
1109 and Hyer, E.: Aerosol optical depth assimilation for a size-resolved sectional
1110 model: impacts of observationally constrained, multi-wavelength and fine mode
1111 retrievals on regional scale analyses and forecasts, *Atmos. Chem. Phys.*, 13,
1112 10425-10444, doi:10.5194/acp-13-10425-2013, 2013.

1113 Schwartz, C. S., Liu, Z., Lin, H. C., and McKeen, S. A.: Simultaneous
1114 three-dimensional variational assimilation of surface fine particulate matter and
1115 MODIS aerosol optical depth, *J. Geophys. Res.*, 117, D13202,
1116 doi:10.1029/2011JD017383, 2012.

1117 Schwartz, C. S., Liu, Z., Lin, H.-C., and Cetola, J. D.: Assimilating aerosol
1118 observations with a “hybrid” variational-ensemble data assimilation system, *J.*
1119 *Geophys. Res. Atmos.*, 119, 4043–4069, doi:10.1002/2013JD020937, 2014.

1120 Sekiyama, T. T., Tanaka, T. Y., Shimizu, A., and Miyoshi, T.: Data assimilation of
1121 CALIPSO aerosol observations, *Atmos. Chem. Phys.*, 10, 39-49,
1122 doi:10.5194/acp-10-39-2010, 2010.

1123 Schutgens, N. A. J., Miyoshi, T., Takemura, T., and Nakajima, T.: Sensitivity tests for
1124 an ensemble Kalman filter for aerosol assimilation, *Atmos. Chem. Phys.*, 10,
1125 6583-6600, doi:10.5194/acp-10-6583-2010, 2010.

1126 Schutgens, N. A. J., Miyoshi, T., Takemura, T., and Nakajima, T.: Applying an
1127 ensemble Kalman filter to the assimilation of AERONET observations in a
1128 global aerosol transport model, *Atmos. Chem. Phys.*, 10, 2561-2576,
1129 doi:10.5194/acp-10-2561-2010, 2010.

1130 Schutgens, N., Nakata, M., and Nakajima, T.: Estimating Aerosol Emissions by
1131 Assimilating Remote Sensing Observations into a Global Transport Model,
1132 *Remote Sensing*, 4, 3528-3543, 2012.

1133 Tang, X., Zhu, J., Wang, Z. F., and Gbaguidi, A.: Improvement of ozone forecast over

1134 Beijing based on ensemble Kalman filter with simultaneous adjustment of initial
1135 conditions and emissions, *Atmos. Chem. Phys.*, 11, 12901–12916,
1136 doi:10.5194/acp-11-12901-2011, 2011.

1137 Tombette, M., Mallet, V., and Sportisse, B.: PM10 data assimilation over Europe with
1138 the optimal interpolation method, *Atmos. Chem. Phys.*, 9, 57-70,
1139 doi:10.5194/acp-9-57-2009, 2009.

1140 Torn, R. D., Hakim, G. J., and Snyder, C.: Boundary conditions for limited-area
1141 ensemble Kalman filters, *Mon. Weather Rev.*, 134, 2490–2502, 2006.

1142 van Loon, M., Builtjes, P. J. H., and Segers, A. J.: Data assimilation of ozone in the
1143 atmospheric transport chemistry model LOTOS, *Environ. Model. Softw.*, 15,
1144 603–609, 2000.

1145 Wang, J., Xu, X., Henze, D. K., Zeng, J., Ji, Q., Tsay, S.-C., and Huang, J.: Top-down
1146 estimate of dust emissions through integration of MODIS and MISR aerosol
1147 retrievals with the GEOS-Chem adjoint model, *Geophys. Res. Lett.*, 39, L08802,
1148 doi:10.1029/2012GL051136, 2012.

1149 Wang, Y. X., Zhang, Q. Q., Jiang, J. K., Zhou, W., Wang, B. Y., He, K. B., Duan, F.
1150 K., Zhang, Q., Philip, S., and Xie, Y. Y.: Enhanced sulfate formation during
1151 China's severe winter haze episode in January 2013 missing from current models,
1152 *J.Geophys.Res.-Atmos.*, 119, 10.1002/2013JD021426, 2014

1153 Wang, X.Y., Liang, X.Z., Jiang, W.M., Tao, Z.N., Wang, J.X.L., Liu, H.N., Han
1154 Z.W., Liu, S.Y., Zhang, Y.Y., Grell, G.A., Peckham, S.E.: WRF-Chem
1155 simulation of East Asian air quality: Sensitivity to temporal and vertical
1156 emissions distributions, *Atmospheric Environment*, 44(2010) 660-669

1157 Whitaker, J. S., and Hamill, T. M.: Ensemble data assimilation without perturbed
1158 observations, *Mon. Weather Rev.*, 130, 1913–1924, 2002.

1159 Woo, J.H., Baek, J.M., Kim, J.W., Carmichael, G.R., Thongboonchoo, N., Kim, S.T.,
1160 An, J.H.: Development of a Multi-Resolution Emission Inventory and Its Impact
1161 on Sulfur Distribution for Northeast Asia, *Water, Air, and Soil Pollution* 148:
1162 259–278, 2003.

1163 Weekly Crop Residue Burning Monitoring Report ,

1164 <http://hjj.mep.gov.cn/jgjs/201510/P020151012746205487305.pdf>, 2015a (in
1165 Chinese).

1166 Weekly Crop Residue Burning Monitoring Report,
1167 <http://hjj.mep.gov.cn/jgjs/201510/P020151019568921489639.pdf>, 2015b(in
1168 Chinese).

1169 Xia Y., Zhao, Y., Nielsen, C.P., Benefits of China's efforts in gaseous pollutant
1170 control indicated by the bottom-up emissions and satellite observations
1171 2000-2014, *Atmospheric Environment*, 136, 43-53, 2016

1172 Yu, H., Dickinson, R. E., Chin, M., Kaufman, Y. J., Geogdzhayev, B., and
1173 Mishchenko, M. I.: Annual cycle of global distributions of aerosol optical depth
1174 from integration of MODIS retrievals and GOCART model simulations, *J.*
1175 *Geophys. Res.*, 108(D3), 4128, doi:10.1029/2002JD002717, 2003.

1176 Yumimoto, K., Uno, I., Sugimoto, N., Shimizu, A., and Satake, S.: Adjoint inverse
1177 modeling of dust emission and transport over East Asia, *Geophys. Res. Lett.*, 34,
1178 L00806, doi:10.029/2006GL028551, 2007.

1179 Yumimoto, K., Uno, I., Sugimoto, N., Shimizu, A., Liu, Z., and Winker, D. M.:
1180 Adjoint inversion modeling of Asian dust emission using lidar observations,
1181 *Atmos. Chem. Phys.*, 8, 2869-2884, doi:10.5194/acp-8-2869-2008, 2008.

1182 Yumimoto, K., Nagao, T.M., Kikuchi, M., Sekiyama, T.T, Murakami, H.,Tanaka,
1183 T.Y., Ogi, A., Irie, H., Khatri, P., Okumura, H., Arai, K., Morino, I., Uchino, O.,
1184 Maki, T.: Aerosol data assimilation using data from Himawari-8, a
1185 next-generation geostationary meteorological satellite, *Geophys. Res. Lett.*, 43,
1186 5886–5894, 2016.

1187 Yin, X.M., Dai, T., Xin, J.Y., Gong, D.Y., Yang, J., Teruyuki, N., Shi, G.Y.:
1188 Estimation of aerosol properties over the Chinese desert region with MODIS
1189 AOD assimilation in a global model, *Adv. Clim. Change Res.*, 7, 90–98, 2016.

1190 Zhang, J., Reid, J. S., Westphal, D., Baker, N., and Hyer, E.: A System for
1191 Operational Aerosol Optical Depth Data Assimilation over Global Oceans, *J.*
1192 *Geophys. Res.*, 113, D10208, doi:10.1029/2007JD009065, 2008.

1193 Zhang, Q., Streets, D. G., Carmichael, G. R., He, K. B., Huo, H., Kannari, A.,

1194 Klimont, Z., Park, I. S., Reddy, S., Fu, J. S., Chen, D., Duan, L., Lei, Y., Wang,
1195 L. T., and Yao, Z. L.: Asian emissions in 2006 for the NASA INTEX-B mission,
1196 Atmos. Chem. Phys., 9, 5131-5153, doi:10.5194/acp-9-5131-2009, 2009.

1197 Zhang, L., Liu, L. C., Zhao, Y. H., Gong, S. L., Zhang, X. Y., Henze, D. K., Capps, S.
1198 L., Fu, T. M., Zhang, Q., and Wang, Y. X.: Source attribution of particulate
1199 matter pollution over North China with the adjoint method, Environ.Res.Lett.,
1200 10, Artn 084011 10.1088/1748-9326/10/8/084011, 2015.

1201 Zheng, B., Zhang, Q., Zhang, Y., He, K. B., Wang, K., Zheng, G.
1202 J., Duan, F. K., Ma, Y. L., and Kimoto, T.: Heterogeneous
1203 chemistry: a mechanism missing in current models to explain
1204 secondary inorganic aerosol formation during the January 2013 haze
1205 episode in North China, Atmos.Chem.Phys., 15, 2031-2049,
1206 10.5194/acp-15-2031-2015, 2015.

1207

1208

1209 **List of Figures and Table**

1210 Figure 1. Locations of 77 PM_{2.5} assimilation observation stations (black dot) and the
1211 77 independent observation stations (red triangle) in the model domain. The three
1212 colored boxes mark sub-regions with relatively dense coverage for the Beijing–
1213 Tianjin–Hebei region (JJJ, 12 assimilation stations and 12 independent stations, red
1214 box), the Yangtze River delta (YRD, 24 assimilation stations and 24 independent
1215 stations, blue box) and the Pearl River delta (PRD, 9 stations and 9 independent
1216 stations, green box).

1217

1218 Figure 2. (a) Framework of M_{SF} and (b) flow chart of the data assimilation system
1219 that simultaneously optimizes the chemical initial conditions and emissions.

1220

1221 Figure 3. Time series of prior ensemble mean RMSE and total spread for PM_{2.5}
1222 concentrations aggregated over all observations over the three sub-regions: (a)
1223 Beijing–Tianjin–Hebei region; (b) Yangtze River delta; (c) Pearl River delta; and (d)
1224 time series of the area mean ensemble spread for $\lambda_{PM2.5}$ over the three sub-regions.

1225

1226 Table 1. Comparison of the surface PM_{2.5} mass concentrations from the control and
1227 assimilation experiments to observations over all analysis times from 6 to 16 October
1228 2014.

1229

1230 Figure 4. Spatial distribution of the PM_{2.5} mass ($\mu\text{g}\cdot\text{m}^{-3}$) of the (a) observations; (b)
1231 simulation of the control run; (c) analysis of expJ; (d) analysis of expC; (e) increments
1232 of expJ; (f) increments of expC; at the lowest model level averaged over all hours
1233 from 6 to 16 October 2014.

1234

1235 Figure 5. Hourly area-averaged time series of emission scaling factors (black)
1236 extracted from the ensemble mean of the analyzed $\lambda_{PM2.5}^a$ and the corresponding
1237 analyzed unspeciated primary PM_{2.5} emissions $E_{PM2.5}^a$ (blue) over the three
1238 sub-regions: (a) Beijing–Tianjin–Hebei region; (b) Yangtze River delta; and (c) Pearl
1239 River delta.

1240

1241 Figure 6. Hourly area-averaged time series of emission scaling factors extracted from
1242 the ensemble mean of the analyzed (a) λ_{NO}^a ; (a) λ_{SO2}^a ; (a) λ_{NH3}^a over the three
1243 sub-regions: Beijing–Tianjin–Hebei region (JJJ, black), Yangtze River delta (YRD,
1244 green), and Pearl River delta (PRD, blue).

1245

1246 Figure 7. Spatial distribution of $\lambda_{PM2.5}$ at the lowest model level averaged over all
1247 hours from 6 to 16 October 2014.

1248

1249 Figure 8. Spatial distribution of (a) the prior unspeciated primary sources of PM_{2.5}
1250 ($\mu\text{g}\cdot\text{m}^{-2}\text{ s}^{-1}$) and (b) the time-averaged differences between the ensemble mean
1251 analysis and the prior values ($\mu\text{g}\cdot\text{m}^{-2}\text{ s}^{-1}$) at the lowest model level averaged over
1252 all hours from 6 to 16 October 2014.

1253

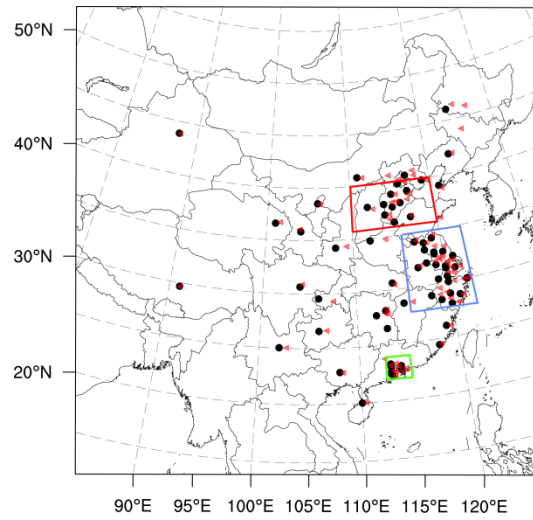
1254 Figure 9. Time series of the hourly PM_{2.5} obtained from observations (circle),
1255 analysis (blue line), control run (black line) and hourly output of 48-h forecast in three
1256 megacities: (a) Beijing; (c) Shanghai; and (e) Guangzhou in expJ and (b) Beijing; (d)
1257 Shanghai; and (f) Guangzhou in expC. See text in section 5.4.

1258

1259 Figure 10. Bias of surface PM_{2.5} as a function of forecast range calculated against
1260 independent observations over the three sub-regions: (a) Beijing–Tianjin–Hebei
1261 region; (c) Yangtze River delta; (e) Pearl River delta and RMSE over (b) Beijing–
1262 Tianjin–Hebei region; (d) Yangtze River delta; (f) Pearl River delta; (g) Normalized
1263 RMSE (assimilation divided by control) for expJ and (h) (g) Normalized RMSE for
1264 expC.

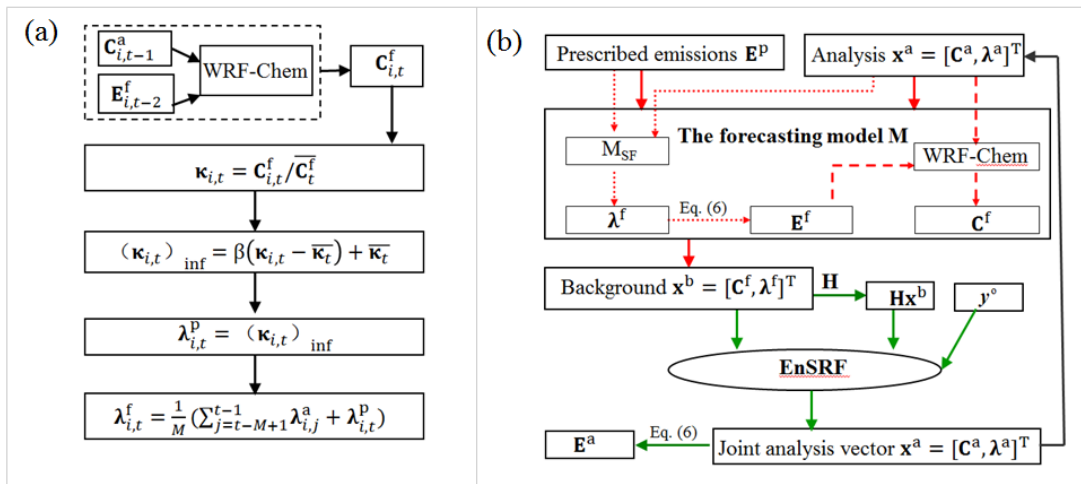
1265

1266
1267
1268



1269
1270
1271
1272
1273
1274
1275
1276
1277

Figure 1. Locations of 77 PM_{2.5} assimilation observation stations (black dot) and the 77 independent observation stations (red triangle) in the model domain. The three colored boxes mark sub-regions with relatively dense coverage for the Beijing–Tianjin–Hebei region (JJJ, 12 assimilation stations and 12 independent stations, red box), the Yangtze River delta (YRD, 24 assimilation stations and 24 independent stations, blue box) and the Pearl River delta (PRD, 9 stations and 9 independent stations, green box).



1279

1280

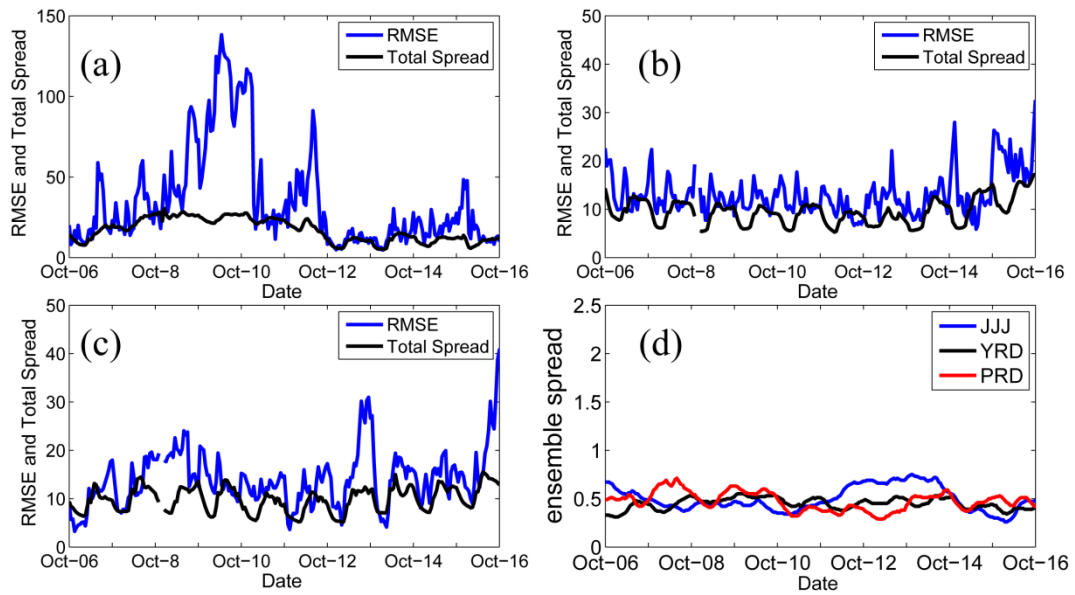
1281

1282

Figure 2. (a) Framework of M_{SF} and (b) flow chart of the data assimilation system that simultaneously optimizes the chemical initial conditions and emissions.

1283

1284



1285

1286

1287

1288

1289

1290

Figure 3. Time series of prior ensemble mean RMSE and total spread for $PM_{2.5}$ concentrations aggregated over all observations over the three sub-regions: (a) Beijing–Tianjin–Hebei region; (b) Yangtze River delta; (c) Pearl River delta; and (d) time series of the area mean ensemble spread for $\lambda_{PM_{2.5}}$ over the three sub-regions.

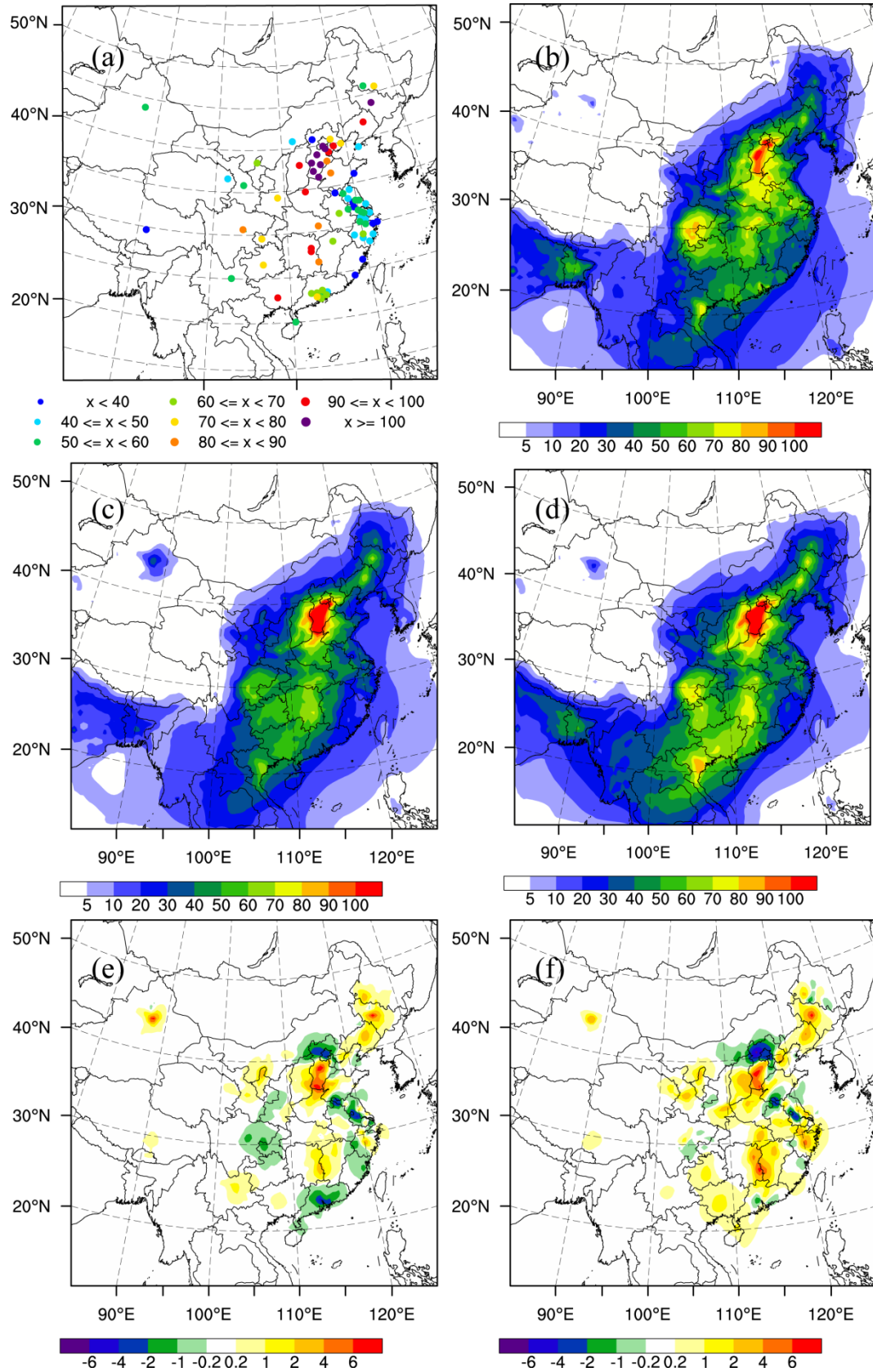
1291

1292 Table 1. Comparison of the surface PM_{2.5} mass concentrations from the control and
 1293 assimilation experiments to observations over all analysis times from 6 to 16 October
 1294 2014.

Region	Experiment	Mean	Mean	BIAS	RMSE	CORR
		observed value	simulated value			
Beijing–	Control		98.3	–18.0	81.6	0.790
Tianjin–	expJ	116.3	106.0	–10.3	66.9	0.827
Hebei	expC		104.1	–12.2	64.0	0.845
Yangtze	Control		64.4	15.9	30.6	0.593
River	expJ	48.5	46.9	–1.6	15.3	0.846
delta	expC		46.1	–2.4	17.3	0.803
Pearl	Control		82.4	20.6	31.8	0.624
River	expJ	61.8	66.5	4.7	16.1	0.800
delta	expC		64.1	–2.3	15.6	0.797

1295

1296



1297

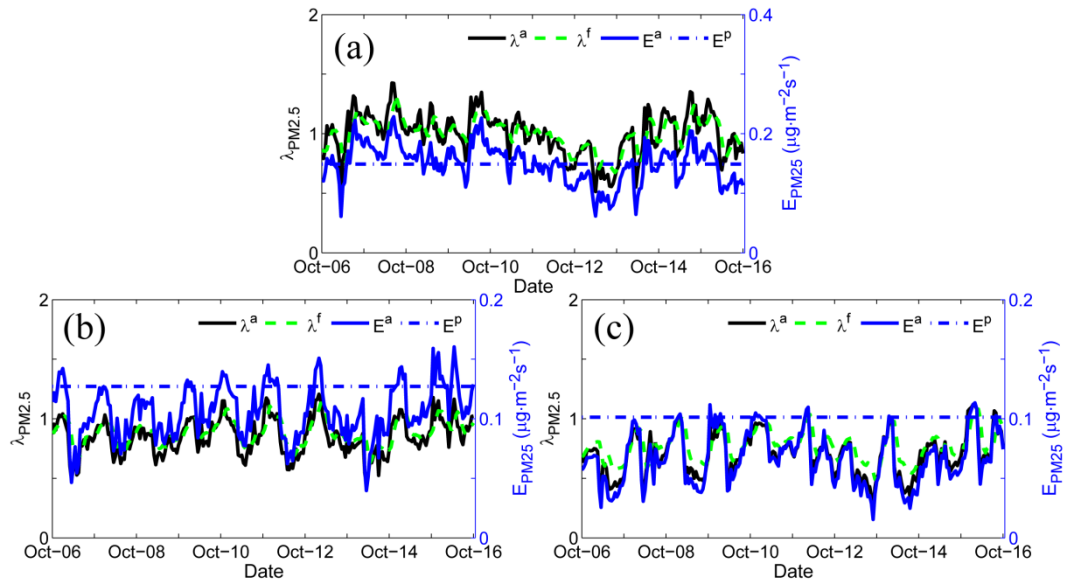
1298

1299

1300

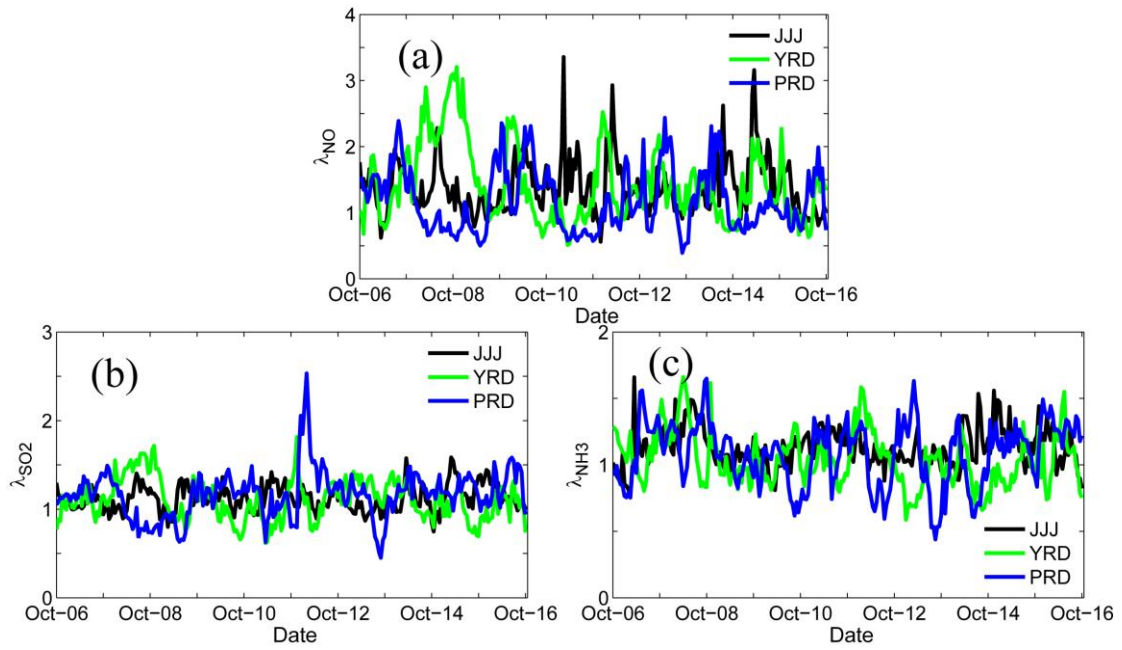
Figure 4. Spatial distribution of the PM_{2.5} mass (μg m⁻³) of the (a) observations; (b) simulation of the control run; (c) analysis of expJ; (d) analysis of expC; (e) increments of expJ; (f) increments of expC; at the lowest model level averaged over all hours

1302
1303
1304



1305
1306
1307
1308
1309
1310
1311

Figure 5. Hourly area-averaged time series of emission scaling factors (black) extracted from the ensemble mean of the analyzed $\lambda_{PM_{2.5}}^a$ and the corresponding analyzed unspesiated primary $PM_{2.5}$ emissions $E_{PM_{2.5}}^a$ (blue) over the three sub-regions: (a) Beijing–Tianjin–Hebei region; (b) Yangtze River delta; and (c) Pearl River delta.



1312

1313

1314

1315

1316

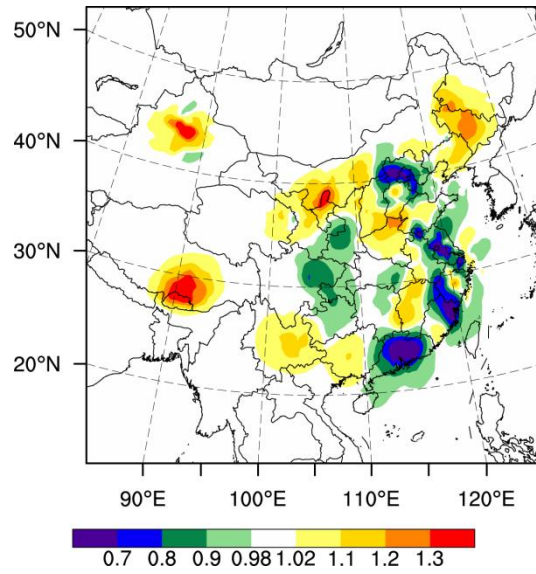
1317

1318

Figure 6. Hourly area-averaged time series of emission scaling factors extracted from the ensemble mean of the analyzed (a) λ_{NO}^a ; (a) $\lambda_{\text{SO}_2}^a$; (a) $\lambda_{\text{NH}_3}^a$ over the three sub-regions: Beijing-Tianjin-Hebei region (JJJ, black), Yangtze River delta (YRD, green), and Pearl River delta (PRD, blue).

1319

1320



1321

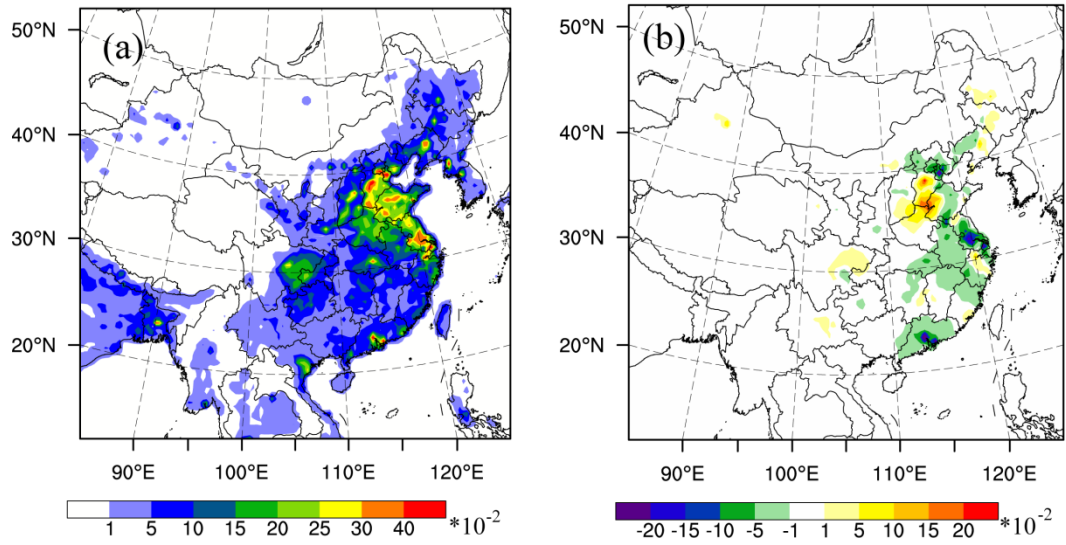
1322

1323

1324

Figure 7. Spatial distribution of $\lambda_{PM2.5}$ at the lowest model level averaged over all hours from 6 to 16 October 2014.

1325

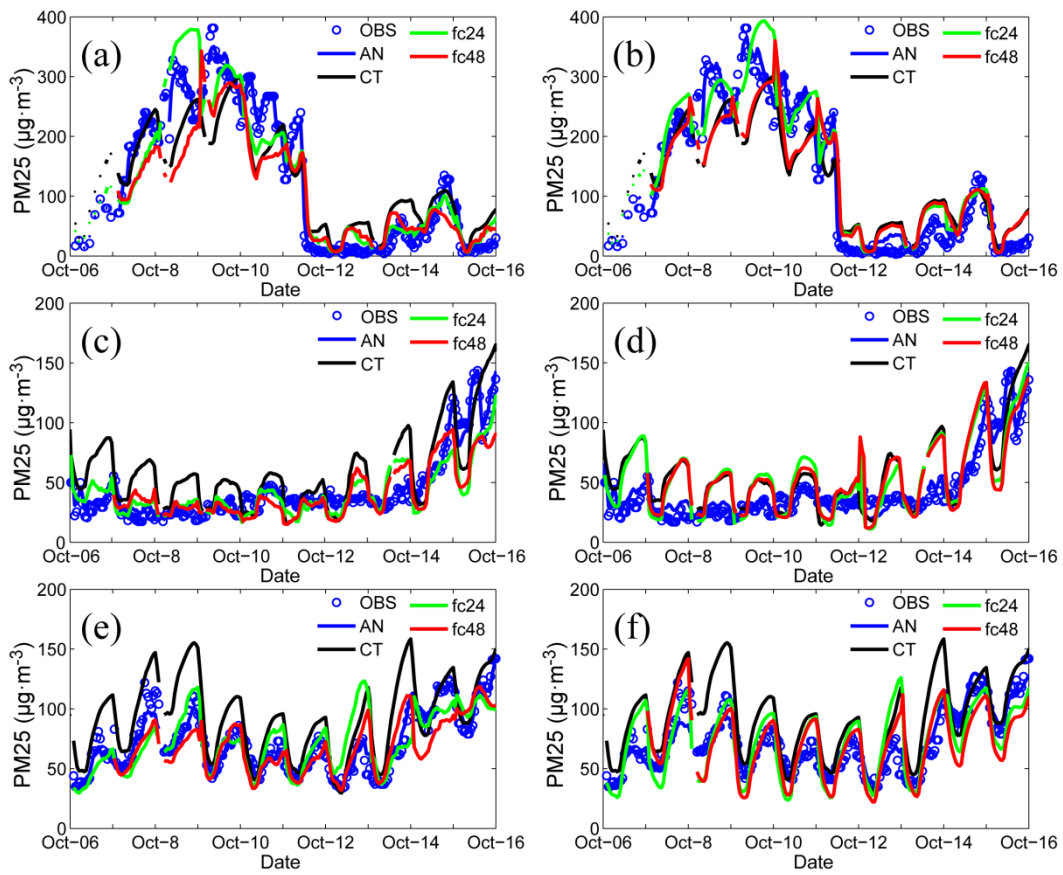


1326

1327 Figure 8. Spatial distribution of (a) the prior unspeciated primary sources of PM_{2.5}
1328 ($\mu\text{g m}^{-2} \text{s}^{-1}$) and (b) the time-averaged differences between the ensemble mean
1329 analysis and the prior values ($\mu\text{g} \cdot \text{m}^{-2} \text{s}^{-1}$) at the lowest model level averaged over all
1330 hours from 6 to 16 October 2014.

1331

1332

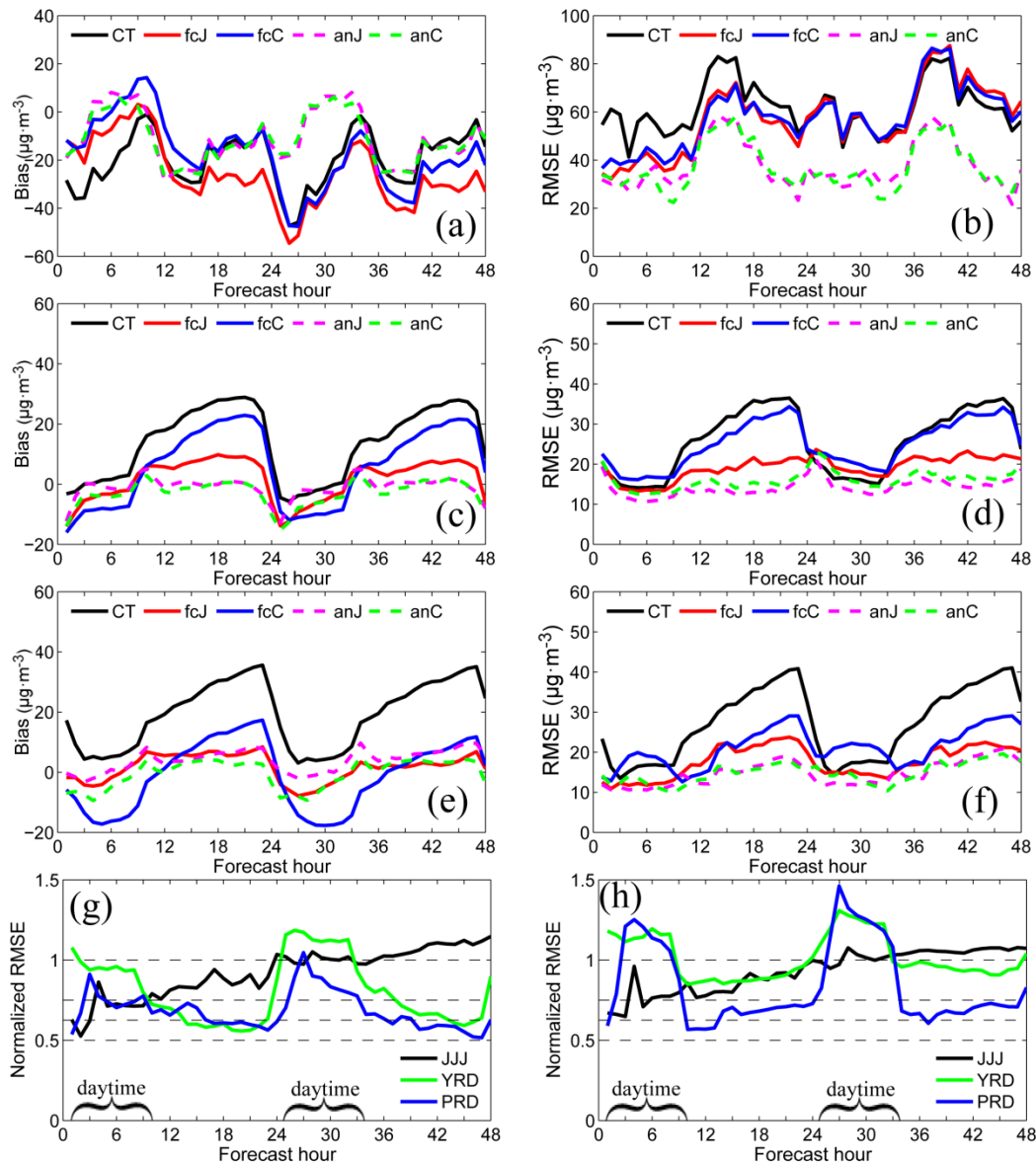


1334

1335 Figure 9. Time series of the hourly PM_{2.5} obtained from observations (circle), analysis
 1336 (blue line), control run (black line) and hourly output of 48-h forecast in three
 1337 megacities: (a) Beijing; (c) Shanghai; and (e) Guangzhou in expJ and (b) Beijing; (d)
 1338 Shanghai; and (f) Guangzhou in expC. See text in section 5.4.
 1339

1340

1341



1342

1343

1344

1345

1346

1347

1348

1349

1350

1351

Figure 10. Bias of surface $\text{PM}_{2.5}$ as a function of forecast range calculated against all the independent observations over the three sub-regions shown in figure 1: (a) Beijing–Tianjin–Hebei region; (c) Yangtze River delta; (e) Pearl River delta and RMSE over (b) Beijing–Tianjin–Hebei region; (d) Yangtze River delta; (f) Pearl River delta; (g) Normalized RMSE (assimilation divided by control) for expJ and (h) Normalized RMSE for expC. The 48-h forecasts were performed at each 0000 UTC from 6 to 16 October 2014 and the statistics were computed from 6 to 16 October.